

# XMM-Newton 13<sup>H</sup> Deep field - I. X-ray sources

N. S. Loaring<sup>1</sup> <sup>★</sup>, T. Dwelly<sup>1</sup>, M. J. Page<sup>1</sup>, K. Mason<sup>1</sup>, I. McHardy<sup>2</sup>, K. Gunn<sup>2</sup>, D. Moss<sup>2</sup>, N. Seymour<sup>3</sup>, A. M. Newsam<sup>4</sup>, T. Takata<sup>5</sup>, K. Sekguchi<sup>5</sup>, T. Sasseen<sup>6</sup>, F. Cordova<sup>7</sup>

<sup>1</sup>MSSL, University College London, Dorking, Surrey, RH5 6NT, UK

<sup>2</sup>School of Physics and Astronomy, University of Southampton, Southampton, SO17 1BJ, UK

<sup>3</sup>Institut d’Astrophysique de Paris, 98bis, Boulevard Arago, 75014 Paris, France

<sup>4</sup>Astrophysics Research Institute, Liverpool John Moores University, Twelve Quays House, Egerton Wharf, Birkenhead, CH41 1LD, UK

<sup>5</sup>National Astronomical Observatory of Japan, 650 North A’ohoku Place, Hilo, HI 96729, USA

<sup>6</sup>Department of Physics, University of California, Santa Barbara, CA 93106, USA

<sup>7</sup>University of California, Riverside, 900 University Avenue, Riverside, CA 92521, USA

1 October 2018

## ABSTRACT

We present the results of a deep X-ray survey conducted with XMM-*Newton*, centred on the UK ROSAT 13<sup>H</sup> deep field area. This region covers 0.18 deg<sup>2</sup> and is the first of two areas covered with XMM-*Newton* as part of an extensive multi-wavelength survey designed to study the nature and evolution of the faint X-ray source population. We have produced detailed Monte-Carlo simulations to obtain a quantitative characterisation of the source detection procedure and to assess the reliability of the resultant sourcelist. We use the simulations to establish a likelihood threshold above which we expect less than 7 (3%) of our sources to be spurious. We present the final catalogue of 225 sources. Within the central 9’, 68 per cent of source positions are accurate to 2” making optical follow-up relatively straightforward. We construct the  $N(> S)$  relation in four energy bands: 0.2-0.5 keV, 0.5-2 keV, 2-5 keV and 5-10 keV. In all but our highest energy band we find that the source counts can be represented by a double powerlaw with a bright end slope consistent with the Euclidean case and a break around  $10^{-14}$  erg cm<sup>-2</sup> s<sup>-1</sup>. Below this flux the counts exhibit a flattening. Our source counts reach densities of 700, 1300, 900 and 300 deg<sup>-2</sup> at fluxes of  $4.1 \times 10^{-16}$ ,  $4.5 \times 10^{-16}$ ,  $1.1 \times 10^{-15}$  and  $5.3 \times 10^{-15}$  erg cm<sup>-2</sup> s<sup>-1</sup> in the 0.2-0.5, 0.5-2, 2-5 and 5-10 keV energy bands respectively. We have compared our source counts with those in the two *Chandra* deep fields and Lockman hole and find our source counts to be amongst the highest of these fields in all energy bands. We resolve > 51% (> 50%) of the X-ray background emission in the 1-2 keV (2-5 keV) energy bands.

**Key words:** surveys - X-ray: selection - background - AGN - cosmology

## 1 INTRODUCTION

It is widely accepted that the majority of the Cosmic X-ray Background (XRB) arises from the integrated emission of discrete extragalactic sources (Schwartz et al. 1976; Giacconi & Zamorani 1987; Maccacaro et al. 1991). The energy density of the XRB peaks at  $\sim$ 30 keV, but the first imaging surveys were carried out at much lower energies:  $<3.5$  keV with *Einstein* and  $<2$  keV with *ROSAT*. By the late 1990s *ROSAT* surveys had resolved 70-80% of the soft XRB, (Shanks et al. 1991; Hasinger et al. 1993, 1998; McHardy et al. 1998). Subsequently, deep XMM-*Newton* and *Chandra* surveys have essentially resolved the soft XRB into discrete sources (Mushotzky et al. 2000; Hasinger et al.

2001; Brandt et al. 2001; Tozzi et al. 2001; Rosati et al. 2002; Alexander et al. 2003). Optical follow up of these sources has revealed a population composed primarily of unobscured broad line active galactic nuclei (AGN), with an increasing fraction of absorbed AGN at fainter fluxes (McHardy et al. 1998; Schmidt et al. 1998; Zamorani et al. 1999; Lehmann et al. 2001; Szokoly et al. 2003; Barger et al. 2003).

In order to investigate further the nature of the obscured population one has to conduct surveys at harder energies ( $>2$  keV), which are less sensitive to absorption. Surveys carried out using ASCA (Georgantopoulos et al. 1997; Cagnoni, Della Ceca & Maccacaro 1998; Ueda et al. 1998, 2001; Ishisaki et al. 2001) and *BeppoSAX* (Fiore et al. 1999; Giommi et al. 2000; Fiore et al. 2001) resolved 25-35% of the XRB above 2 keV. More recently, the XMM-*Newton* and *Chand-*

<sup>★</sup> ns1@mssl.ucl.ac.uk

*dra* deep field surveys have resolved 60-90% of the hard (>2 keV) X-ray background (Hasinger et al. 2001; Giacconi et al. 2001; Tozzi et al. 2001; Cowie et al. 2002; Rosati et al. 2002; Alexander et al. 2003; Manners et al. 2003) probing fluxes a factor 100× fainter than the *ASCA* and *BeppoSAX* surveys. The wide range in resolved fraction arises not only due to the variation in source counts between the surveys, but also due to the uncertainty of the absolute normalisation of the hard XRB, for example the *BeppoSAX* XRB normalisation from Vecchi et al. (1999) is ∼30% higher than the *ASCA* value from Gendreau et al. (1995).

Optical follow up studies of the deepest surveys find a predominance of  $z < 1$  objects which do not show broad emission lines (Barger et al. 2001; Tozzi et al. 2001; Barger et al. 2002; Lamer et al. 2003; Barger et al. 2003). There is an increasing contribution from normal galaxies at the faintest fluxes, and it appears likely that normal galaxies will outnumber AGN below 0.5-2 keV fluxes of  $10^{-17}$  erg cm $^{-2}$  s $^{-1}$  (Bauer et al. 2004). A significant fraction of the hard X-ray sources in these fields are optically faint, with  $R > 24$  and are therefore difficult to identify optically (Alexander et al. 2001; McHardy et al. 2003; Alexander et al. 2003).

Despite the great advances made in detecting increasingly fainter X-ray sources, the physical nature and evolution of the faint hard X-ray population remains largely unknown. The redshift distribution and column density distribution of the absorbed AGN are still poorly constrained.

Another issue which needs addressing is the relationship between gas and dust absorption in AGN. There have been several cases of a mismatch between optical and X-ray classifications, indicating a wide range in dust/gas ratios for obscured sources (Akiyama et al. 2000; Page et al. 2001; Comastri et al. 2001; Maiolino et al. 2001a; Loaring et al. 2003; Carrera et al. 2004).

In particular, high quality X-ray spectra are needed to determine the dominant X-ray emission mechanisms and the amount of absorption. We have therefore used *XMM-Newton* to carry out deep surveys of two widely separated fields to probe the X-ray population down to fluxes  $\sim 10^{-15}$  erg cm $^{-2}$  s $^{-1}$  in the 0.5-2 and 2-5 keV energy bands. The source counts in these energy bands exhibit a break at  $\sim 10^{-14}$  erg cm $^{-2}$  s $^{-1}$  (Rosati et al. 2002) around which the maximum contribution to the XRB per logarithmic flux interval occurs.

This paper presents the X-ray catalogue derived from the first of these two *XMM-Newton* surveys, carried out in the UK *ROSAT* deep field area (hereafter the 13<sup>H</sup> deep field). The field has also been observed with a mosaic of *Chandra* pointings which cover the whole *XMM-Newton* field of view and provide accurate source positions. It is complemented with multiwavelength follow up in the UV, optical, near-IR, mid-IR and radio (Seymour et al. 2004). The *Chandra* catalogue has already been presented elsewhere (McHardy et al. 2003); here we present the *XMM-Newton* catalogue and observed source counts.

## 2 OBSERVATIONS AND DATA REDUCTION

### 2.1 XMM observations

The 13<sup>H</sup> deep field is centred on the sky co-ordinates RA 13h 34m 37.1s, Dec +37° 53' 02.2" (J2000). The *XMM-Newton* observations were carried out in three separate revolutions during June 2001 for a total exposure time of 200 ks. The European Photon

Imaging Cameras (EPICs Turner et al. 2001) were operated in standard full-frame mode. The thin filter was used for the PN camera, while the thin and medium filters were alternated for the MOS1 and MOS2 cameras. Table 1 gives a summary of the observations.

The data were processed using the *XMM-Newton* Standard Analysis System (SAS) version 6.0. Approximately 40% of the total observation time was affected by high particle background flares, arising from soft protons hitting the detector. The data were therefore temporally filtered to remove these high background periods. In practice, times where the 5-10 keV count rates exceeded 2 s $^{-1}$  in the MOS cameras and 4 s $^{-1}$  in the PN camera were excluded. Filtering reduced the total useful exposure time from ∼200 ks to ∼120 ks. The net live times for the individual detectors after the periods of high background were excised are listed in Table 1.

A significant component of the EPIC background comes from instrumental emission lines, in particular the Cu K $\alpha$  line at 8.1 keV in the PN and the Al K $\alpha$  line at 1.5 keV in both detectors (Lumb et al. 2002). Events with energies close to those of the emission lines were filtered out to minimise the instrumental contribution to the background. Events in bad columns, bad pixels and adjacent to chip edges were also excluded.

Images and exposure maps were then constructed from each observation for each detector in four energy bands: 0.2-0.5 keV, 0.5-2 keV, 2-5 keV and 5-10 keV. Single-pixel events were used to construct the PN 0.2-0.5 keV image. Single, double and triple events were used to construct the higher energy PN images. For MOS, all valid event patterns were used to construct the images regardless of energy band. In each energy band, the exposure maps were scaled to the PN thin filter response. The images and exposure maps from the different detectors and observations were then summed to produce one image and one exposure map per energy band. The response-weighted summation over each observation and telescope gives total on-axis PN-equivalent live exposure times of 152 ks, 161 ks, 179 ks, and 160 ks, in the 0.2-0.5 keV, 0.5-2 keV, 2-5 keV, and 5-10 keV bands respectively.

For the EPIC imaging observing modes, photons are not only registered during the actual integration interval but also during the readout of the CCD. These out-of-time events are hence assigned the wrong position in the readout direction. The fraction of out-of-time events is highest for the PN full frame mode (6.3 %) and therefore for each PN exposure, an additional synthetic out-of-time events list was produced by randomising the coordinates of the events within each chip in the readout direction. Out-of-time images were constructed in each energy band by filtering these event lists in exactly the same way as the real event lists. These out-of-time images were used as inputs to the background model as described in Section 2.2.

The astrometry of the individual observations was corrected for small offsets between the pointings. A sourcelist was constructed for each observation as described in Section 2.2 and cross-correlated with the optical positions of the 214 sources found in the *Chandra* catalogue of McHardy et al. (2003) using the SAS task EPOS COR. The appropriate offsets in RA and dec were then applied to each of the individual events to tie the *XMM-Newton* data to the optical/*Chandra*/radio co-ordinate frame. The images and exposure maps were then reproduced with the correct astrometry. The actual offsets in RA and Dec differed slightly between the three observations. The first observation (revolution 276, 179 *XMM-Newton* sources) had offsets of 1.4", -1.3" applied, the second (revolution 281, 106 *XMM-Newton* sources) had offsets of 0.5", -0.5" applied and the third observation (revolution 282, 257 *XMM-Newton* sources) had offsets of 0.6", 0.2" applied.

Rev.	Date	Live Time (ks)			Filter	
		MOS1	MOS2	PN	MOS1	MOS2
276	12.06.01	43.1	45.8	35.5	thin	med
281	22.06.01	14.1	12.0	6.7	med	thin
282	23.06.01	59.2	60.2	47.9	thin	thin

**Table 1.** Summary of  $13^H$  deep field XMM-Newton observations showing the date and length of observations and the filters used. The live times have had periods of high background excluded.

## 2.2 XMM-Newton Source detection

The combined images in each energy band were source-searched simultaneously using the SAS tasks EBOXDETECT and EMLDETECT. EBOXDETECT is a sliding cell detection algorithm which outputs an initial sourcelist. This sourcelist is input for the EMLDETECT task which performs a maximum likelihood PSF fit to the sources producing refined positions and fluxes for all bands simultaneously. This method results in better source positions than searching in the individual energy bands one at a time because the PSF fit is based on the maximum number of counts per source. If the best fit source count rate in any particular energy band is less than zero (i.e. there are fewer counts at the source position in the image than in the background map) the source count rate is set to zero in this energy band.

A background map was produced for each combination of observation, detector and energy band (36 background maps in total) using our own software. This software performs a maximum likelihood fit to the background, assuming a three-component background model: out-of-time events, a flat unvignetted component, caused primarily by cosmic rays, and a vignetted component representing unresolved faint sources and genuinely diffuse emission. For the PN, the out-of-time events contribution to the background was fixed at 6.3% of the intensity of the synthetic out-of-time images; for the MOS background, we assumed no contribution from out-of-time events. The intensities of the vignetted and unvignetted background components were free parameters in the fit.

To maximise sensitivity an iterative procedure was employed. Initially, sources were detected in each individual image (per detector and per energy band) using a 3-pixel-square sliding cell in EBOXDETECT, with the background computed as the average of the surrounding  $7 \times 7$  pixels. Then, the sources were excised from the individual images and the background fitted. Each of the background maps from the MOS and PN cameras for a given energy band were then summed to produce one combined background map for each energy band. The resultant background maps were then used for the sliding cell (EBOXDETECT) followed by maximum likelihood (EMLDETECT) source detection on the combined image in each energy band. The sequence of background determination followed by source searching was then repeated several times. We found that the sourcelist and background maps converged after 4 iterations. Likelihood thresholds (DET\\_ML values output from the source detection) of 4 and 5 were chosen for EBOXDETECT and EMLDETECT respectively. These values are related to the probability of a random Poissonian fluctuation having caused the observed source counts via (Cash 1979):

$$\text{DET\_ML} = -\ln P_{\text{random}} \quad (1)$$

The conversion factors from count rates to flux were determined from the EPIC response matrices, over exactly the same energy ranges as those in which the images were constructed, assum-

Energy (keV)	ECF ( cts per $10^{-11}$ erg cm $^{-2}$ )
0.2–0.5	4.7775
0.5–2.0	4.8905
2.0–5.0	1.9605
5.0–10.0	0.5929

**Table 2.** Energy conversion factors (ECF) used to convert between count rate and flux.

ing a power law spectrum with photon index  $\Gamma = 1.7$ . This is a good average within our flux range (Page et al. 2003; Mateos et al. 2005); however the sources have a range of photon indices. To assess the impact of such a spread we have calculated the expected conversion factors using photon indices of  $\Gamma = 1.4$  and  $\Gamma = 2.0$  respectively. This range represents the expected spread in spectral slope for sources contributing to the XRB. The relatively flat  $\Gamma = 1.4$  lower limit corresponds to the XRB slope in the 3–15 keV range, produced by absorbed AGN. The upper limit value is typically found in unabsorbed AGN, and we would therefore expect the bulk of our sources to lie between the two values.

The largest effect is in the 0.2–0.5 keV and 5–10 keV energy bands where the conversion factors derived are different from those assuming a photon index of  $\Gamma = 1.7$  by up to 11% and 8% respectively. However, in the 0.5–2 and 2–5 keV bands the photon index chosen only affects the conversion factors by 1–2%. The PN response matrices include only single and double pixel events, but for the three highest energy bands our PN images also include triple and quadruple events. In order to take this into account, the count rate to flux conversion factors were corrected (by up to 6% in the hardest band) as described in Osborne et al. (2001).

## 3 MONTE CARLO FIELD SIMULATION

We have used an XMM-Newton specific extension of the simulation method of Hasinger et al. (1998) to obtain a quantitative characterisation of the source detection procedure and to assess the reliability of the resultant sourcelist. We have used our simulations to find the appropriate detection threshold to be applied to the  $13^H$  field. A Monte-Carlo approach is particularly powerful near the survey flux limit where a number of different processes contribute to uncertainties in the detected source parameters. Our simulation method consists of several modular steps that are repeated for a large number of synthetic fields. Briefly, an ‘input’ sourcelist was generated independently in each energy band. Each list was then folded through the XMM-Newton imaging characteristics to generate images in each energy band. These images were then source searched to produce ‘output’ sourcelists. A pairing algorithm was used to associate an ‘input’ source with each ‘output’ source. Each of these stages are described in detail in Appendix A. Here we present the results of a comparison between the output and input source properties. These provide an indication of the biases inherent in our survey. One thousand simulated fields were used to reduce statistical uncertainties in the analysis.

### 3.1 Comparison of simulated input and output sources

In order to assess the accuracy of source positions and fluxes, and to estimate the degree to which confusion and Eddington bias affects the source counts in our  $13^H$  data we have compared the input and

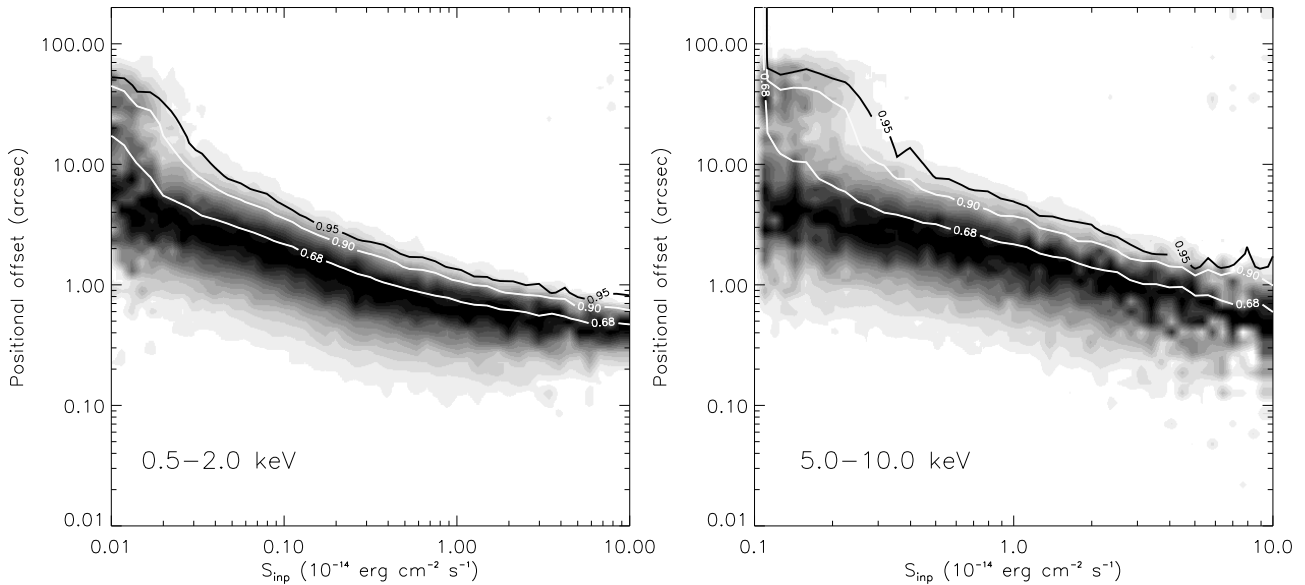


**Figure 1.** Greyscale images showing the distribution of positional offsets between output and input source locations as a function of input flux in two energy bands. Those sources within the central  $9'$  of the XMM-Newton field of view having  $\text{DET\_ML} \geq 5$  are shown. The concentration of positional offsets as a function of  $S_{\text{inp}}$  is indicated by the darkness of the greyscale image. The three contours show the distances within which 68, 90, and 95 per cent of the data lie.

output properties of our simulations. The simulations should mimic any biases found in the real data.

We matched each output source found in the simulated images to the closest valid input source. We consider an input source as valid when its flux,  $S_{\text{inp}}$ , contributes a reasonable fraction ( $>20$  per cent) to the total output flux,  $S_{\text{out}}$ . No upper limit was applied to the radius at which input and output sources were matched in order to assess the typical offsets between input and output positions. Fig. 1 shows the distribution of measured positional offsets as a function of input flux,  $S_{\text{inp}}$ . The greyscale image shows the relative density of sources at a given  $S_{\text{inp}}$ . The dark band shows where the majority of sources lie. All sources with  $\text{DETML} > 5$  and offaxis angles  $< 9'$  are shown. The contour lines plotted correspond to the positional offsets within which 68, 90 and 95 per cent of the data lie.

The mean positional offset decreases with increasing flux and is  $< 10''$  for all but the faintest fluxes. In the 0.5–2 keV energy band, 95 per cent of sources with  $S_{\text{inp}} > 5 \times 10^{-16} \text{ erg cm}^{-2} \text{ s}^{-1}$  and offaxis angles  $\leq 9'$  have positional offsets  $< 10''$ . In the 5–10 keV energy band, 95 per cent of sources with  $S_{\text{inp}} > 5 \times 10^{-15} \text{ erg cm}^{-2} \text{ s}^{-1}$  and offaxis angles  $\leq 9'$  have positional offsets  $< 10''$ . Those with offaxis angles  $> 9'$  have systematically larger positional offsets (larger by  $\sim 2''$  over the majority of flux ranges). Any sources with higher positional offsets are most likely due to incorrect associations. A discussion of the positional accuracy found in the real  $13^H$  data and its comparison with the simulations is deferred to Section 4.3.

Subsequently, we matched output sources to input sources within a radius  $r_{\text{cut}} = 5'', 8'',$  and  $10''$  for offaxis angles of  $0 - 9'$ ,  $9 - 12'$  and  $> 12'$  respectively, reflecting the degradation of the XMM PSF (Kirch 2004) away from the optical axis. Where more than one candidate input source lay within  $r_{\text{cut}}$ , the brightest was chosen. The brightest input candidate within  $r_{\text{cut}}$  must be the ‘correct’ input counterpart in the sense that it is the largest contributor to the output source counts. In practice, when averaged over the

1000 simulations, only 0.6, 1.7, 1.5 and 0.5 output sources per field had more than one valid ( $5S_{\text{inp}} \geq S_{\text{out}}$ ) input candidate within  $r_{\text{cut}}$  in the 0.2–0.5, 0.5–2.0, 2.0–5.0, and 5.0–10 keV energy bands.

The output fluxes and positions were then compared with the corresponding input values. There are several reasons why we might expect a difference between the input and output flux distributions and source counts: i) a systematic or statistical flux measurement inaccuracy, ii) source confusion, iii) statistical fluctuations in the background which may be detected as sources, and iv) Eddington bias. All these factors must be considered together when interpreting the  $13^H$  field data.

The intrinsic accuracy of the source detection photometry is best evaluated at high fluxes and low offaxis angles, where ii), iii) and iv) are less important. The bright end of Fig. 2 illustrates the high fidelity of the detected fluxes,  $S_{\text{out}}$ , to the input fluxes,  $S_{\text{inp}}$ . Considering sources with  $S_{\text{inp}} > 5 \times 10^{-14} \text{ erg cm}^{-2} \text{ s}^{-1}$ , with offaxis angles  $< 9'$  the average  $S_{\text{out}}/S_{\text{inp}}$  ratio is  $1.01 \pm 0.03$  ( $1\sigma$ ) in energy bands 0.2–0.5, 0.5–2 and 2–5 keV. In our highest energy band the average  $S_{\text{out}}/S_{\text{inp}}$  ratio is also 1.01 but the scatter is larger ( $1\sigma = 0.06$ ).

The distribution of  $S_{\text{out}}/S_{\text{inp}}$  is shown in Fig. 3 for three flux intervals in each energy band. At bright fluxes ( $S_{\text{inp}} = 2 \times 10^{-14} \text{ erg cm}^{-2} \text{ s}^{-1}$ ) the distribution is narrow, symmetrical and centred on  $S_{\text{out}}/S_{\text{inp}} = 1$ , because the statistical errors on the fluxes are small. At intermediate fluxes ( $S_{\text{inp}} = 6 \times 10^{-15} \text{ erg cm}^{-2} \text{ s}^{-1}$ ) the distributions are still relatively symmetrical, but they are slightly broader as the statistical errors on the fluxes are larger. However, at the faintest fluxes, the distributions are much broader and significantly skewed towards larger  $S_{\text{out}}/S_{\text{inp}}$  ratios. The increased width is due to the increased statistical errors on the fluxes. The distributions are shifted towards larger  $S_{\text{out}}/S_{\text{inp}}$  ratios because at such faint fluxes sources are unlikely to be detected unless they are enhanced by Poisson fluctuations or by source confusion.

Source confusion occurs when two or more nearby input sources fall in a single resolution element of the detector and re-

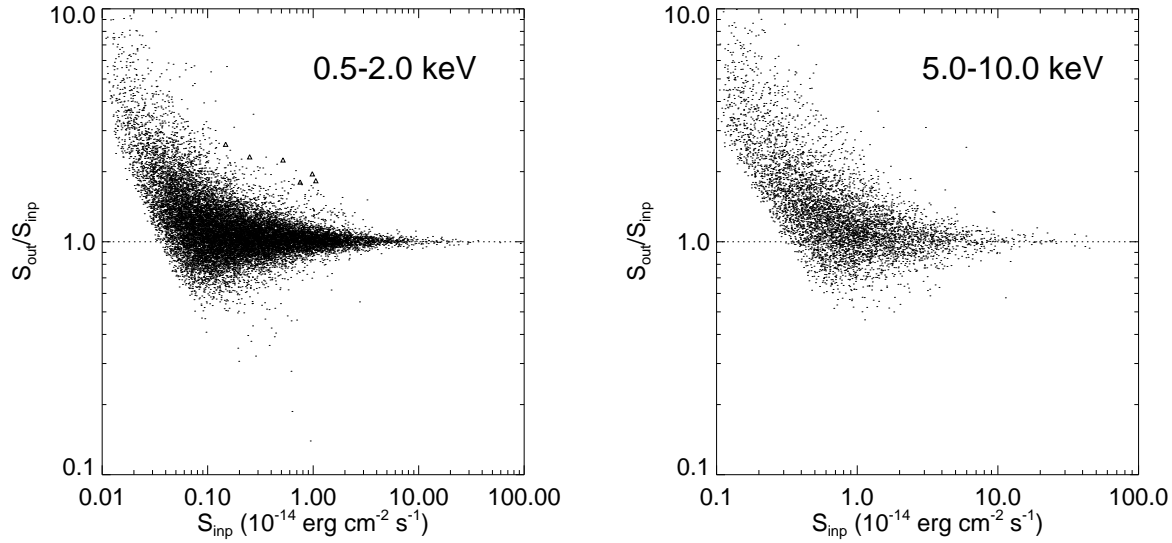


**Figure 2.** Scatter plots of input vs output flux in two selected energy bands. We only show those detected sources having  $\text{DET\_ML} \geq 5$  and input counterparts within  $5'', 8'',$  and  $10''$  for input offaxis angles of  $0 - 9'$ ,  $9 - 12'$  and  $> 12'$  respectively. Sources with  $S_{\text{out}}/(S_{\text{inp}} + 3\sigma_{\text{out}}) > 1.5$  are plotted as triangles. The results for 100 simulations are shown for clarity.

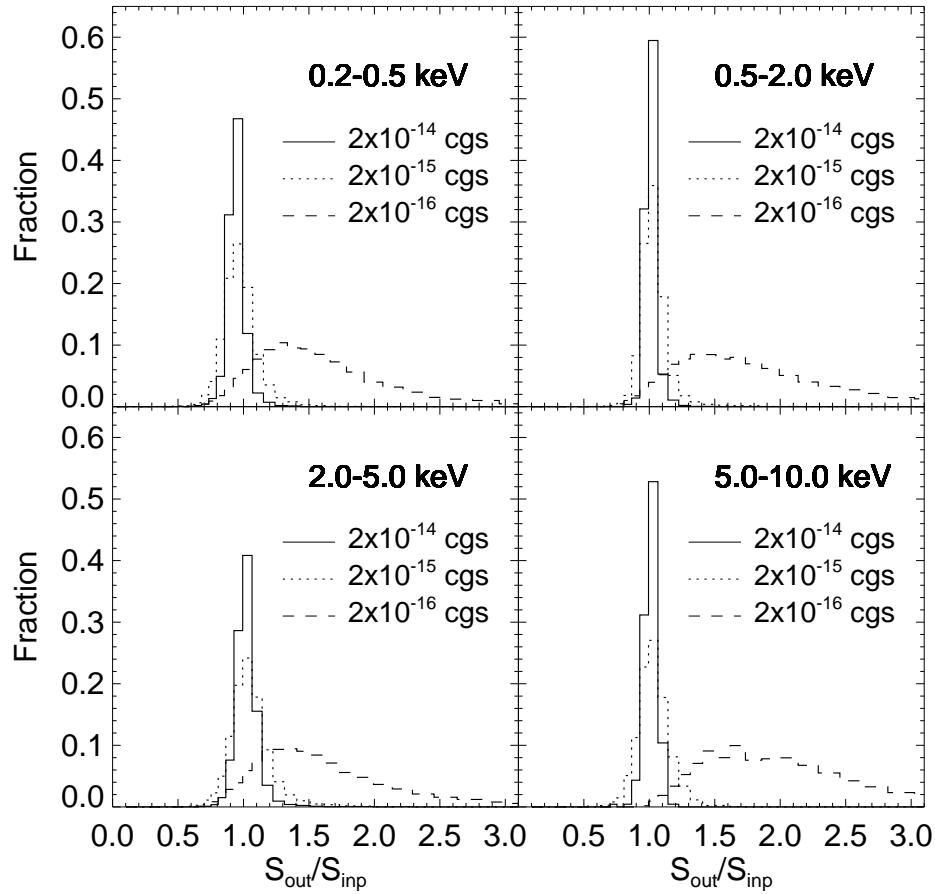


**Figure 3.** The distribution in output ( $S_{\text{out}}$ ) flux to input flux ( $S_{\text{inp}}$ ) ratio for three illustrative input flux ranges. The solid line represents the sources in the flux interval centred on  $S_{\text{inp}} = 2 \times 10^{-14} \text{ erg cm}^{-2} \text{ s}^{-1}$  ( $1 \times 10^{-14} - 4 \times 10^{-14} \text{ erg cm}^{-2} \text{ s}^{-1}$ ). The dotted line represents sources in the flux interval centred on  $S_{\text{inp}} = 6 \times 10^{-15} \text{ erg cm}^{-2} \text{ s}^{-1}$  ( $3 \times 10^{-15} - 1.2 \times 10^{-14} \text{ erg cm}^{-2} \text{ s}^{-1}$ ) and the dashed line represents sources in the flux interval centred on  $S_{\text{inp}} = 4 \times 10^{-16} \text{ erg cm}^{-2} \text{ s}^{-1}$  ( $2 \times 10^{-16} - 8 \times 10^{-16}$ ). The flux intervals were chosen such that  $\Delta \log S_{\text{inp}} = 0.3$ .

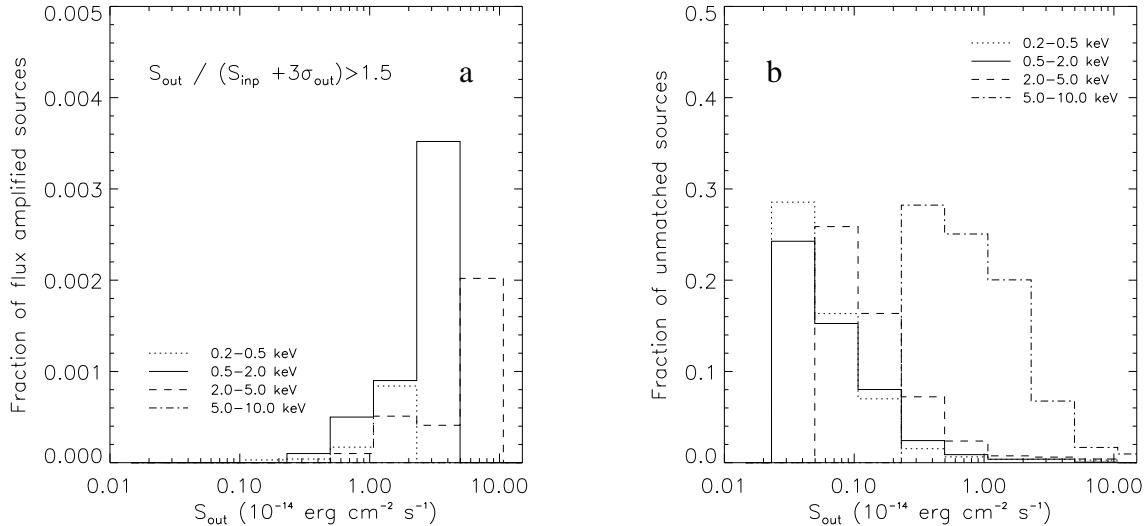


**Figure 4.** a) Fraction of flux amplified sources as a function of flux. b) Fraction of unmatched sources as a function of flux. (0.2–0.5 keV (dotted), 0.5–2 keV (solid), 2–5 keV (dashed), 5–10 keV (dot-dashed)). The fraction of flux amplified sources is < 0.4 per cent in all energy bands and is significantly less than the fraction of unmatched sources.

sult in a single output source. This results in a flux amplification in the output source and a net loss of fainter sources. The position of the output source will be close to the centroid of the merged input sources. Therefore when two input sources of similar flux are confused, the output position does not correspond to either of the input positions. Source confusion can limit the depth of any deep survey depending on the size of the telescope beam, and on the sky-density of objects as a function of flux. In practice, we cannot distinguish between a source boosted by photon noise or one confused with another faint source, therefore we consider the two effects jointly. We class sources as ‘flux amplified’ (corresponding to ‘confused’ sources in Hasinger et al. 1998) if  $S_{out}/(S_{inp} + 3\sigma_{out}) > 1.5$  (where  $\sigma_{out}$  is the  $1\sigma$  error on the output flux  $S_{out}$ ). Fig. 4a shows the fraction of flux amplified sources as a function of input flux in our four energy bands. The fraction is less than 0.4 per cent at all fluxes in all energy bands. This fraction will depend on the exact definition of flux amplification. Using a less stringent definition of  $S_{out}/(S_{inp} + 3\sigma_{out}) > 1.2$  still results in a fraction well below 2% in each energy band at all fluxes.

We class an output source as ‘unmatched’ when there are no valid ( $S_{out} \leq 5S_{inp}$ ) input sources within  $r_{cut}$  (corresponding to ‘spurious’ sources in Hasinger et al. 1998). These are mainly caused by positive fluctuations in the background. Fig. 4b shows the fraction of unmatched sources as a function of flux in each energy band. As expected, the unmatched fraction is highest at very faint fluxes, where up to 30% of the sources are unmatched. Unmatched sources are many times more numerous than the flux amplified sources at any flux.

In our simulations we curtailed our input sourcelists at fluxes  $5\times$  fainter than those found in the  $13^H$  data in each energy band in order to speed up processing time. In order to assess the impact of the simulation flux limit on the number of flux amplified and spurious sources, we have also produced a smaller number of simulations to a greater depth, reaching fluxes  $10\times$  fainter than those found in the  $13^H$  data. The fraction of flux amplified sources in

these faint simulations agrees with the fraction found in our original simulations to within 0.02 per cent. Likewise, the fraction of unmatched sources agrees to within 2 per cent. We are therefore satisfied that our chosen flux limits are sufficiently deep.

In order to investigate the flux limits at which confusion noise dominates over Poisson errors, we have produced and source-searched a small number of ultra-deep simulations with no Poisson noise. The results are presented and discussed in Appendix B, and show that the  $13^H$  flux limits are more than a factor of 4 brighter than the ultimate XMM-Newton confusion limit in any of the 4 energy bands.

Eddington bias (Eddington 1913) results in a systematic offset in the number of sources detected at a given flux. The magnitude of this effect depends on the both the statistical errors on the measured flux values and on the intrinsic slope of the  $N(S)$ . As there are generally many more faint sources than bright ones, uncertainties on the measured flux values will result in more faint sources being up-scattered than bright sources being down-scattered. Therefore we would expect more faint sources to be detected than are actually input, and the output source counts at a given flux to be greater than those input. In the case of our simulations the situation is further complicated due to the double powerlaw form of the  $N(S)$  distribution and the fact that the flux error distribution is non-uniform and a function of several parameters including flux and offaxis angle.

The level of Eddington bias expected in the  $13^H$  deep field is shown in Fig. 5 where the simulated input and output source counts are compared. Below  $S_{knee}$  the ratio rises as the statistical errors on the flux measurements increase. At the lowest flux interval there is a drop in output source counts. The reason for this is the strong skew in  $S_{out}/S_{inp}$  at the faintest fluxes (see Fig. 3) which boosts the output fluxes. The output/input source counts ratio is a minimum at  $S_{knee}$  where both the statistical errors on the flux measurement are low and the source counts become flat. Above  $S_{knee}$  the output/input source count ratio is constant within the errors with a value of  $\sim$

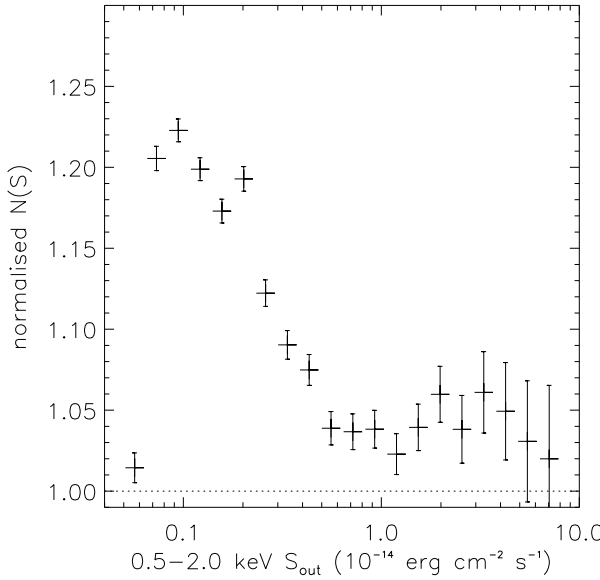


**Figure 5.** Simulated output (crosses) 0.5–2 keV  $N(S)$  distribution normalised by the input distribution. The error bars represent Poisson errors on the output source counts. The dotted line represents the case where the input and output source counts are equal. The source counts are most disparate at faint fluxes where the output counts are enhanced by up to 23%.

1.05 indicating that Eddington bias affects our bright counts at the 5% level.

### 3.2 Assessing the reliability of the $13^H$ sources

In this section we describe how we determined from our simulations the appropriate detection threshold to be applied to the  $13^H$  field EMLDETECT sourcelist. Our aim was to produce a sourcelist such that nearly all erroneous detections are removed whilst retaining the maximum number of real sources.

For each detected source, EMLDETECT measures the detection maximum likelihood statistic, DET<sub>ML</sub>, which takes account of source counts, background counts, and the PSF. For the real data, the SAS task EMLDETECT provides both single-band and multi-band measurements of DET<sub>ML</sub>. For the simulated images we are limited to single band measurements as the four bands are simulated independently. To simulate all four bands simultaneously would require *a priori* knowledge of the sources' intrinsic X-ray spectra, redshifts and column densities which we do not have. The value of DET<sub>ML</sub> for any single detection is directly related to the probability of the source being caused by a random Poisson fluctuation via Eqn. 1. However, it is difficult to translate a minimum threshold value of DET<sub>ML</sub> applied to the whole sourcelist into a total number of expected spurious sources in the field as the probability is a function of position within the field, due to the varying PSF and exposure map. This is therefore best explored via a large number of Monte-Carlo simulations.

Using the simulated sourcelists in each band, we calculated the fraction of sources which were either flux amplified or unmatched as a function of the minimum detection threshold DET<sub>ML</sub><sub>min</sub>. This is shown in Fig. 6. To restrict the fraction of bad sources in our final  $13^H$  sourcelist we use the value of DET<sub>ML</sub><sub>min</sub> in each band at which only 5 percent of sources are either flux am-

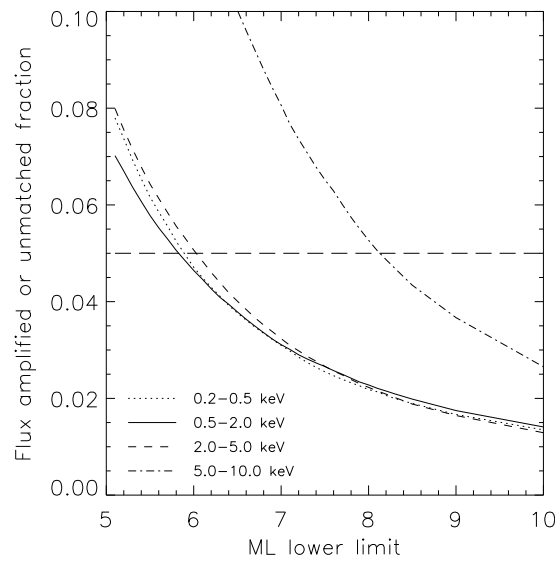


**Figure 6.** Plot showing the fraction of flux amplified or unmatched sources for a range of lower DET<sub>ML</sub> limits. Results are shown for each energy band, 0.2–0.5keV (large dash), 0.5–2keV (solid line), 2–5keV (small dash), 5–10keV (dot-dash). The dotted line shows the 5% badness level.

plified or unmatched in our simulations; these are 5.9, 5.9, 6.0, 8.1 in the 0.2–0.5, 0.5–2, 2–5, and 5–10 keV bands respectively. For a source to pass our significance threshold we require that it has DET<sub>ML</sub>  $\geq$  DET<sub>ML</sub><sub>min</sub> in *at least* one energy band. In practice, because we use a multi-band source detection process for the  $13^H$  data, we expect fewer than 5% bad sources after we have applied this criterion, as many of the sources will be detected in more than one energy band.

For each source in the  $13^H$  sourcelist, we can identify all the output sources from the simulations which lie within 2' of the real  $13^H$  source and have a similar DET<sub>ML</sub> (within 10%). The fraction of these output sources which are unmatched or flux amplified gives a good estimate of the probability that the detection of the real source in this energy band is unreliable. For sources detected in more than one band the probability that the source is spurious is given by the product of these individual probabilities. The total number of spurious sources expected in the  $13^H$  field can then be estimated by summing the probabilities from each source.

### 3.3 Maximum likelihood $N(S)$ fitting method

Our simulations are ideal for testing our  $N(S)$  fitting procedure because we know *a priori* the input  $N(S)$  fitting parameters. Accurate fitting of any  $N(S)$  relation requires a knowledge of the sky area searched and the probability of detection at a given flux. In Fig. 7 the effective area of the survey as a function of limiting flux is shown for each energy band. This was determined by comparing the number of output to input sources at each flux and multiplying the resultant fraction by the geometric area of the survey. Additionally, the distribution of  $S_{out}/S_{inp}$  is required to account for Eddington bias (see Fig. 3, and Section 3.1).

Adapting the maximum likelihood method of Murdoch et al. (1973), we fitted a double powerlaw model to the output  $N(S)$  relation. Rather than fitting the observed fluxes directly, we

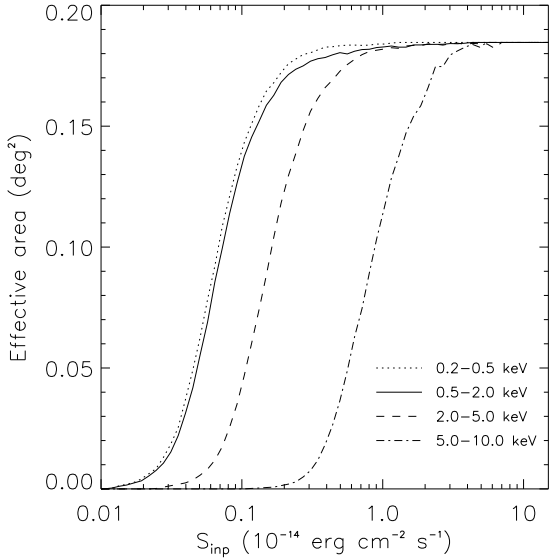


**Figure 7.** Effective area for each energy band, determined from Monte-Carlo simulations (0.2–0.5 keV (dotted), 0.5–2 keV (solid), 2–5 keV (dashed), 5–10 keV (dot-dashed)).

convolved a model  $N(S)$  with the distribution of  $S_{out}/S_{inp}$  to produce a model probability distribution of observed fluxes  $P(S_{out})$ . The best-fit  $N(S)$  was then determined by maximising the likelihood of obtaining the observed flux distribution. As a check, we applied this technique to our simulated data, and recover the input values to within the statistical limits of our simulations ( $\sim 2\%$ ). We are therefore confident in applying this technique to the real  $13^H$  data. Fits neglecting the distribution of  $S_{out}/S_{inp}$  are typically systematically offset by  $\sim 5\%$ .

## 4 RESULTS

In this section we present our final source catalogue and results of fits to our source counts. We compare the properties of our sources with those detected by *Chandra* in the same area and closely examine our quoted positional uncertainties via comparisons with both *Chandra* detections and our simulations.

### 4.1 X-ray source catalogue

Following the source detection procedure described in Section 2.2 (simultaneous source searching in four energy bands), a total of 275 sources were detected with  $DET\_ML > 5$  in at least one energy band. This sourcelist was curtailed using the  $DET\_ML_{min}$  values for each energy band determined in Section 3.2. This reduced the final number of sources to 225. The final sourcelist is presented in Table 9. Using the procedure described in Section 3.2 we expect a total of 7 spurious sources.

### 4.2 $13^H$ deep field source counts

We show the *integral*  $N(> S)$  in each energy band in Fig. 8. We have fitted single and double powerlaw models to the unbinned differential source counts in all energy bands using the method described in Section 3.3. The four identified Galactic stars in the field

Energy (keV)	$\gamma$	$K$	KS Prob
0.2–0.5	$1.84^{+0.20}_{-0.18}$	$47 \pm 20$	$1.8 \times 10^{-2}$
0.5–2.0	$1.69^{+0.11}_{-0.11}$	$112 \pm 23$	$1.0 \times 10^{-10}$
2.0–5.0	$1.91^{+0.20}_{-0.19}$	$126 \pm 28$	$3.5 \times 10^{-4}$
5.0–10.0	$2.80^{+0.67}_{-0.55}$	$150 \pm 18$	$2.9 \times 10^{-5}$

**Table 3.** Best-fit values for a single powerlaw fit to the  $13^H$  deep field differential source counts. All errors are at 95% confidence. The best-fit slope,  $\gamma$ , is listed together with the normalisation,  $K$ , in units of  $(10^{-14} \text{ erg cm}^{-2} \text{ s}^{-1})^{\gamma-1} \text{ deg}^{-2}$ . KS null-hypothesis probabilities on the fits are listed in the final column.

have been excluded from this analysis. The best-fit double powerlaw models are overlaid in Fig. 8 (single powerlaw in the 5–10 keV energy band) as solid lines. The 95% confidence interval of the fits are indicated by the bowties. These incorporate errors on the slopes, normalisations and knee if applicable.

The best-fit parameters for a single powerlaw fit are listed in Table 4.2. The uncertainties on the fit parameters are quoted at the 95% confidence interval for one interesting parameter. We have tested the goodness of fit of these models using the Kolmogorov-Smirnov (KS) test, and the null-hypothesis probabilities that we obtain are given in Table 4.2. The fits are unacceptable in all bands.

For the double powerlaw fits we have fixed the slope at bright fluxes ( $\gamma_2$ ) and fit only for the slope at faint fluxes ( $\gamma_1$ ) and knee position ( $S_{knee}$ ). In the 0.2–0.5 keV band we set  $\gamma_2 = 2.51$  based on results from the *ROSAT* All Sky Survey (Voges et al. 1999). The value of  $\gamma_2$  in the 0.5–2 keV band was fixed at 2.60, derived from the RIXOS survey (Mason et al. 2000). For the 2–5 keV band  $\gamma_2$  was fixed at 2.65 as found in the *BeppoSAX* High Energy Large Area Survey (HELLAS Giommi et al. 2000), and consistent with the ASCA derived value of 2.5 from Ueda et al. (1999). The fit parameters for the double powerlaw fits are listed in Table 4. The double powerlaw model provides a better fit compared to a single powerlaw model in each of these three energy bands. However, the double powerlaw model fit is formally rejected with 99% confidence in the 0.5–2 and 2–5 keV energy bands. In all three energy bands  $S_{knee}$  occurs between  $1.08 - 1.27 \times 10^{-14} \text{ erg cm}^{-2} \text{ s}^{-1}$ .

In the 5–10 keV band the slope found in the single powerlaw fit is consistent with that found by Baldi et al. (2002) at brighter fluxes. We attempted to fit a double powerlaw model to the 5–10 keV band source counts, but in this case  $S_{knee}$  is unconstrained. We therefore consider that a double powerlaw model for the source counts is not justified at the depth of our survey in this energy band.

### 4.3 Positional uncertainties

To assess the reliability of the EMLDETECT positional errors in the *XMM-Newton* sourcelist we have cross-correlated the final *XMM-Newton* and *Chandra* sourcelists. The spread in positional offsets between the two catalogues should provide a good representation of the true spread in *XMM-Newton* positional errors. To prevent the (albeit small) statistical errors on the *Chandra* positions contributing to the spread, where possible we used the position of the optical counterpart to the *Chandra* source: the positional errors on the optical counterparts are typically less than  $0.3''$  (McHardy et al. 2003). The two sourcelists were matched within a search radius of  $10''$  over the entire *XMM-Newton* field of view.

The two catalogues have 155 sources in common. The positional offset between the 155 matched *XMM-Newton* and *Chandra*

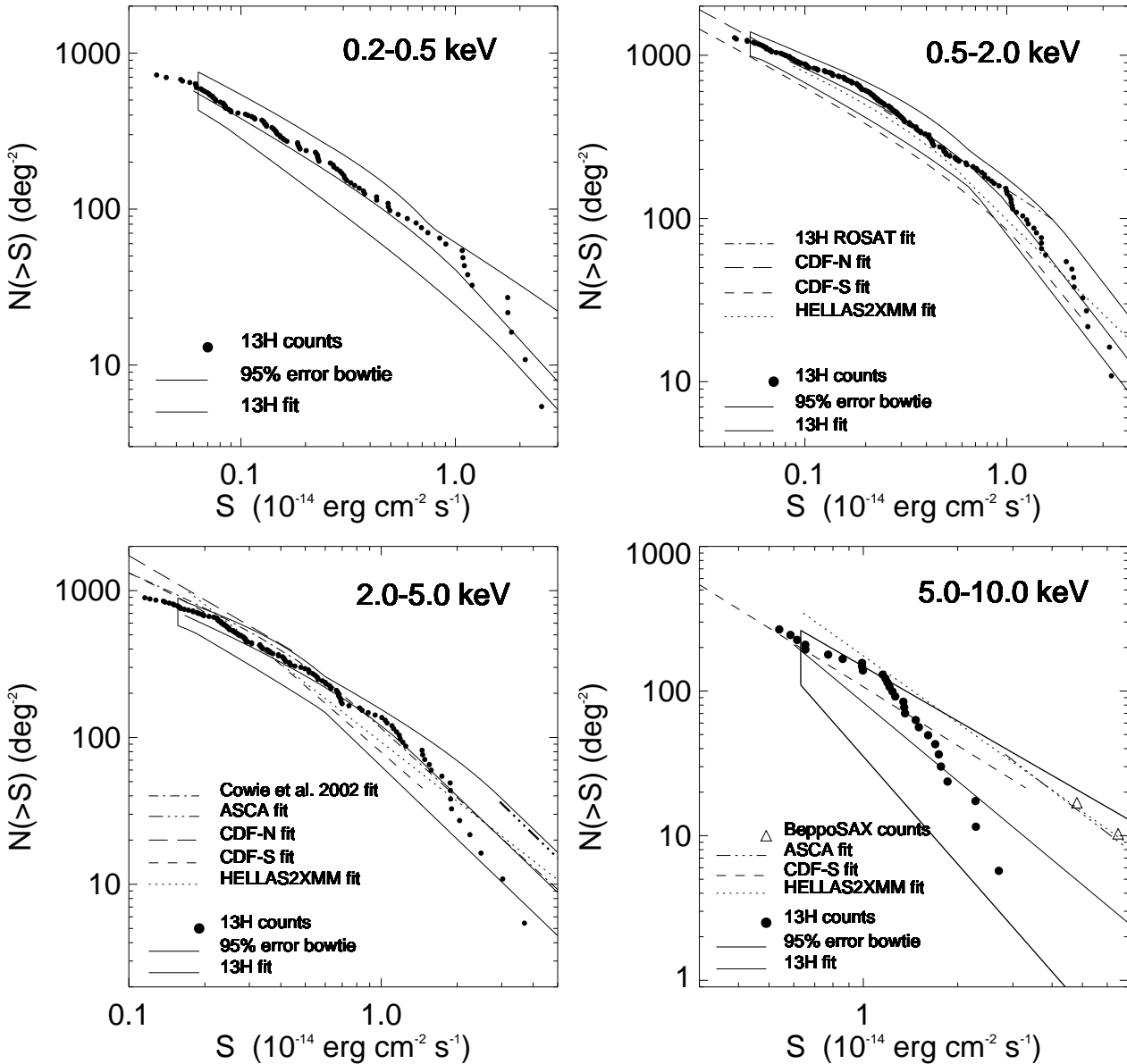


**Figure 8.**  $13^H$  deep field integral  $N(>S)$  in each energy band. Bowties indicate 95% errors. Overlaid for comparison are the results from the CDF-S (dash) (Rosati et al. 2002), CDF-N (long dash) (Brandt et al. 2001), HELLAS2XMM (dot) (Baldi et al. 2002) and ASCA (dot-dot-dot-dash) (Cagnoni, Della Ceca & Maccacaro 1998) surveys. In the 0.5–2.0 keV band the ROSAT counts found in the  $13^H$  field (McHardy et al. 1998) are also overlaid (dot-dash). In the 2–5 keV band the results from Cowie et al. (2002) are also overlaid (dot-dash). Triangles in the 5–10 keV band denote the BeppoSAX counts of Fiore et al. (2001).

Energy (keV)	$\gamma_1$	$\gamma_2$	$S_{knee}$	$K_1$	$K_2$	KS Prob
0.2–0.5	$1.74^{+0.25}_{-0.26}$	2.51	$1.16^{+11.08}_{-0.69}$	$56 \pm 23$	$62 \pm 88$	$7.7 \times 10^{-2}$
0.5–2.0	$1.41^{+0.19}_{-0.18}$	2.60	$1.08^{+1.02}_{-0.39}$	$183 \pm 51$	$201 \pm 67$	$6.4 \times 10^{-5}$
2.0–5.0	$1.66^{+0.30}_{-0.47}$	2.65	$1.27^{+1.66}_{-0.70}$	$163 \pm 94$	$207 \pm 76$	$1.5 \times 10^{-2}$

**Table 4.** Best-fit parameters for a double powerlaw fit to the  $13^H$  differential source counts. The slopes and normalisations below and above the break flux,  $S_{knee}$  are denoted by  $\gamma_1$  and  $\gamma_2$  respectively. The values of  $\gamma_2$  in the three energy bands were fixed to appropriate values found from the literature. The break flux,  $S_{knee}$  is in units of  $10^{-14} \text{ erg cm}^{-2} \text{ s}^{-1}$ . Normalisations  $K_1$  and  $K_2$  are in units of  $(10^{-14} \text{ erg cm}^{-2} \text{ s}^{-1})^{\gamma-1} \text{ deg}^{-2}$ . All errors are at 95%. KS null-hypothesis probabilities on the fits are listed in the final column.

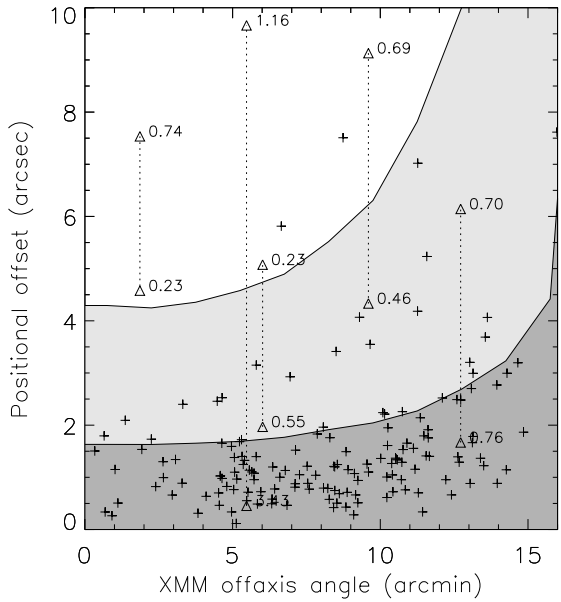


**Figure 9.** Positional offsets between XMM-Newton and *Chandra* counterparts as a function of XMM-Newton offaxis angle. Triangles denote XMM-Newton detections with  $> 1$  *Chandra* counterparts within  $10''$  (numbers indicate the XMM-Newton flux in units of  $10^{-14}$  erg cm $^{-2}$  s $^{-1}$ ). The shaded areas indicate the regions where 68% (dark grey) and 95% (light grey) of the simulated data lie. In the case of the simulations the positional offset is that between the input and output source. 86% of the  $13^H$  data lies within the 68% simulation contour, indicating that the real data have better source positions. This is due to the fact that the real data are generally detected in  $> 1$  energy band.

sources as a function of XMM-Newton offaxis angle is shown in Fig. 9. The positional offsets increase with XMM-Newton offaxis angle, but 80 per cent of the matched sources have positional offsets  $\leq 2''$ ; 95 per cent of the sources have positional offsets  $\leq 4''$ .

We compared this distribution with that found from the simulations (see Section 3.1) which should provide a good indication of the distribution of positional offsets arising within the source detection chain. The contours in Fig. 9 show the distribution of differences between input and output source positions in the 0.5–2 keV simulations. The dark (light) grey area shows where 68% (95%) of the simulated sources lie. The distribution of XMM-Newton - *Chandra* offsets is more highly peaked than the input-output offsets in our simulations: 86% of XMM-Newton - *Chandra* offsets lie within the 68% simulation contour. This is because the real sources in the  $13^H$  field are generally detected in more than one energy band, contrary to the simulated sources. Fitting the source positions in all four energy bands simultaneously, as was done to produce our source catalogue, results in better positional accuracy than a single band fit because more source counts are used in the fit.

Five of the matched sources have more than one *Chandra* counterpart. However, in two out of the five cases, the closest counterpart is significantly brighter than the other one, and we are easily able to identify the correct counterpart. This suggests that  $\sim 2\%$  of our sources are confused, in broad agreement with the fraction of flux amplified sources expected from our simulations.

In Fig. 10 we plot the statistical positional uncertainties of the XMM-Newton sources given by EMLDETECT against the actual positional uncertainties given by the XMM-Newton - *Chandra* offsets. These are compared with our 0.5–2 keV simulation distribu-

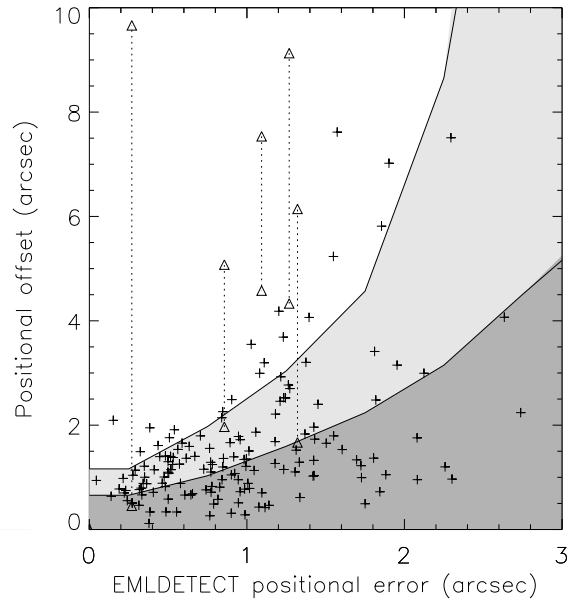


**Figure 10.** Positional offsets between XMM-Newton and *Chandra* counterparts compared with quoted XMM-Newton positional error. The shaded areas indicate the regions where 68% (dark grey) and 95% (light grey) of the simulated data lie. In the case of the simulations the positional offset is that between the input and output source. 43% of the  $13^H$  data lie within the 68% simulation contour indicating that EMLDETECT underestimates the true positional error.

tions where in the case of the simulations the positional offsets are those of the input/output source positions. The dark (light) grey areas show where 68% (95%) of the simulated sources lie. In general, the positional offsets are slightly larger than the EMLDETECT errors for the  $13^H$  data. However, for EMLDETECT positional errors less than  $1''$  the positional offsets have a broader distribution in the  $13^H$  data than in the simulations: only 43% of the  $13^H$  data lies within the 68% simulation region. This implies that the EMLDETECT positional error in the  $13^H$  field underestimates the true positional error. We have therefore added in quadrature a systematic error to the statistical EMLDETECT positional error of each  $13^H$  source, such that 68% of the  $13^H$  sources lie within the 68% region of the simulations. This is achieved with an additional systematic positional error of  $0.76''$  ( $1\sigma$ ). This additional component may be due to residual uncertainties in the detector geometry and may represent a fundamental limit to the accuracy of *any* XMM-Newton position. According to our simulations, EMLDETECT positional errors greater than  $\sim 2.5''$  may underestimate the true positional error by an order of magnitude (the 95% simulation region limit samples a non-gaussian tail at this point) and should be used with this caveat in mind. Section 5.2 further discusses the reliability of the survey and the implications of the positional uncertainties.

#### 4.4 Comparisons with *Chandra* detections

There are 70 XMM-Newton sources with no *Chandra* counterpart. Of these, 9 sources are either on the very edge or out of the field of view of the *Chandra* mosaic (see McHardy et al. 2003) and would therefore not be expected to have a *Chandra* counterpart. R-band images, centred on the positions of these 70 sources are presented in Fig. 11. (Optical images of those sources with a *Chandra* counterpart are presented in McHardy et al. 2003). In 49 cases there is a

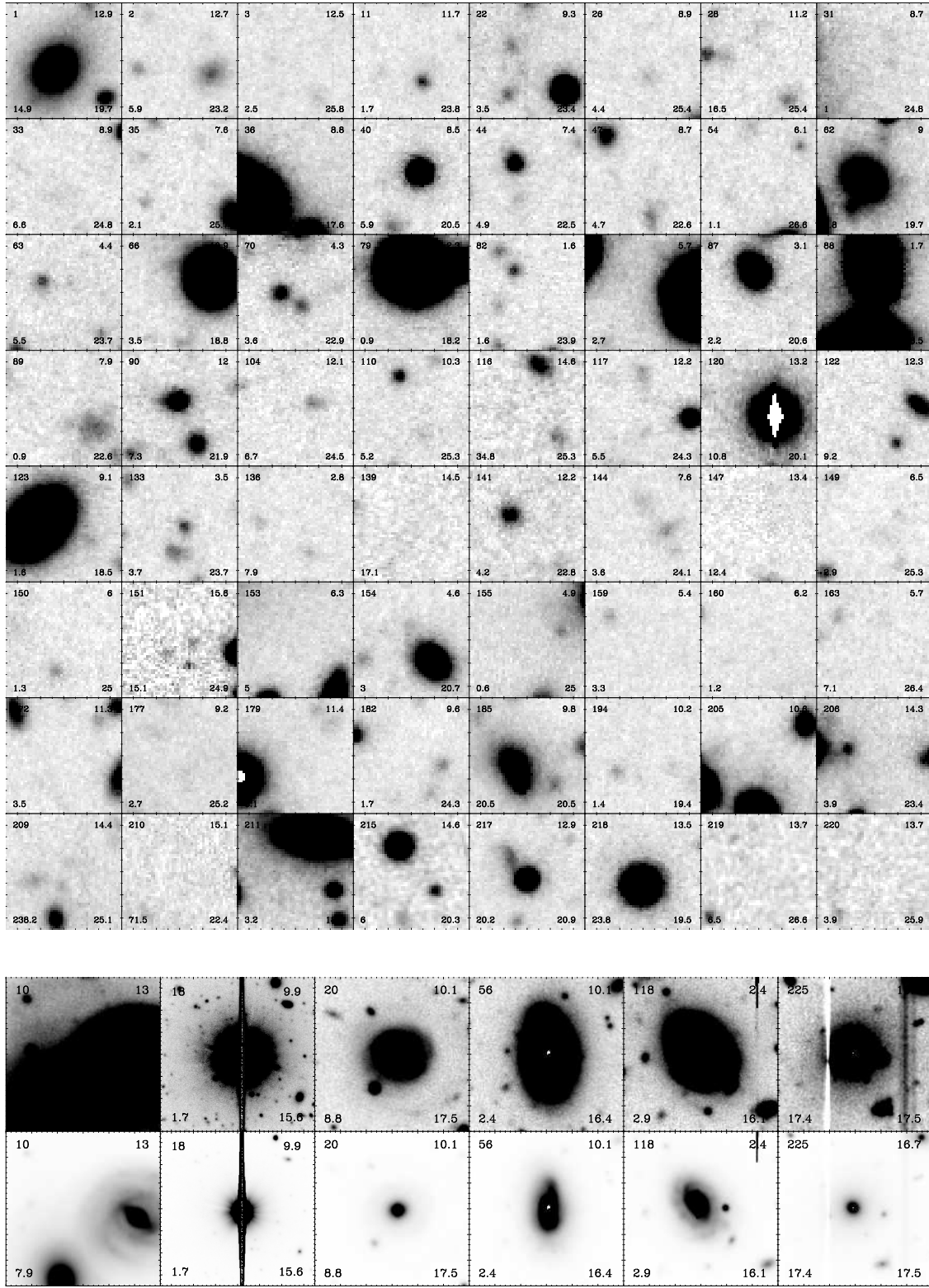


**Figure 11.** Top:  $10'' \times 10''$   $R$ -band Subaru SuprimeCam images centred on the XMM-Newton sources without *Chandra* counterparts. The XMM-Newton reference number (shown in column 1 of Table 9) is at the top left of each image. The XMM-Newton off-axis angle is at the top right. The XMM-Newton  $0.2 - 10$  keV flux (in units of  $10^{-15}$  erg cm $^{-2}$  s $^{-1}$ ) is at the bottom left and the optical counterpart  $R$  magnitude, if applicable, is given in the bottom right. All of these SuprimeCam images have the same greyscale levels to ease comparison of the optical counterparts' brightnesses. The greyscale was chosen to correspond to that in McHardy et al. (2003). Bottom:  $30'' \times 30''$   $R$ -band Subaru SuprimeCam images centred on the 6 XMM-Newton sources with *Chandra* counterparts which are too extended to fit in a  $10'' \times 10''$  box. Source number 18 is actually shown in a  $70'' \times 70''$  box. The top images are at the same grey scale level as Fig. 11. The lower images have their grey scales adjusted for maximum contrast. Source number 10 is not listed as having an optical counterpart in Table 5 as the centre of the barred spiral galaxy is outside the error circle of the XMM-Newton source. However, we may be seeing X-ray emission from an X-ray source in the spiral arms of the galaxy.

XMM-Newton No.	RA J(2000)	Dec J(2000)	Pos. err. (arcsec)	Offaxis (arcmin)	0.2-10.0 keV Flux	Extension	R mag.	Chandra counts	Faint Chandra source?	Comments
1	13 33 28.96	37 55 58.82	1.57	12.91	14.86	—	19.74	3	n	
2	13 33 30.32	37 56 12.21	2.38	12.67	5.94	—	23.18	1	n	
3	13 33 30.68	37 55 05.57	3.04	12.53	2.55	—	25.83	0	n	
10	13 33 38.91	38 01 56.15	4.83	12.96	7.88	—	0.00	0	n	
11	13 33 40.70	37 49 47.79	1.99	11.74	1.65	—	23.76	2	n	
18	13 33 43.80	37 54 55.76	2.56	9.95	1.74	—	15.63	3	y	
20	13 33 45.45	37 58 08.04	0.92	10.14	8.82	—	17.45	0	n	
22	13 33 47.52	37 53 51.51	1.11	9.27	3.46	—	23.39	1	n	
26	13 33 50.80	37 57 16.61	1.77	8.88	4.43	—	25.41	3	y	
28	13 33 54.21	38 02 53.17	1.23	11.21	16.49	—	25.41	0	n	
31	13 33 57.90	37 49 59.01	2.91	8.70	0.98	—	24.79	1	n	
33	13 33 58.87	38 00 24.88	1.18	8.87	6.60	—	24.83	1	n	
35	13 33 59.56	37 51 39.75	2.34	7.57	2.06	—	25.69	2	n	
36	13 33 59.63	37 49 26.35	12.19	8.75	1.86	—	17.64	0	n	
40	13 34 01.06	38 00 25.75	1.50	8.55	5.92	—	20.50	1	n	
44	13 34 07.18	37 59 59.34	1.23	7.36	4.87	—	22.50	0	n	
47	13 34 08.39	37 47 50.85	2.69	8.72	4.67	—	22.65	1	n	
54	13 34 12.36	37 59 10.36	2.01	6.06	1.10	—	26.57	1	n	
56	13 34 13.59	37 45 39.06	1.22	10.12	2.42	—	16.43	3	y	
62	13 34 15.49	38 03 05.78	1.80	8.97	4.81	—	19.68	2	n	
63	13 34 15.54	37 52 27.80	1.31	4.43	5.54	—	23.65	2	y	
66	13 34 17.80	37 44 31.39	2.04	10.89	3.51	—	18.76	2	y	
70	13 34 19.56	37 51 47.77	1.40	4.26	3.58	—	22.89	0	y	Possible faint source outside error circle
79	13 34 22.70	37 55 23.49	2.15	2.32	0.90	—	18.17	3	n	
82	13 34 25.91	37 54 59.90	1.58	1.64	1.63	—	23.94	2	n	
83	13 34 26.87	38 00 27.92	1.45	5.73	2.66	—	0.00	1	n	
87	13 34 28.66	37 57 48.26	1.92	3.09	2.21	—	20.64	3	y	
88	13 34 28.80	37 53 37.96	1.78	1.67	2.15	—	18.46	0	n	
89	13 34 29.20	38 02 45.33	1.79	7.90	0.89	—	22.56	0	n	
90	13 34 29.30	38 06 51.45	1.76	11.98	7.29	—	21.88	1	n	Edge of Chandra FOV
104	13 34 34.92	38 07 03.03	1.99	12.13	6.71	—	24.47	3	n	
110	13 34 36.38	38 05 14.02	1.25	10.32	5.16	—	25.32	4	y	
116	13 34 38.83	37 40 22.03	1.11	14.58	34.78	—	25.30	0	n	Outside Chandra FOV
117	13 34 38.96	37 42 43.95	1.60	12.22	5.49	—	24.30	0	n	
118	13 34 39.75	37 57 01.93	1.29	2.38	2.91	—	16.14	4	y	
120	13 34 42.29	37 41 46.46	0.78	13.24	10.84	—	20.14	0	n	Outside Chandra FOV
122	13 34 42.81	37 42 42.62	1.55	12.33	9.25	—	0.00	0	n	Edge of Chandra FOV
123	13 34 42.84	38 03 53.27	2.33	9.13	1.65	—	18.53	1	n	
133	13 34 47.18	37 57 14.88	1.53	3.46	3.71	—	23.73	4	y	
136	13 34 48.22	37 54 14.33	1.06	2.85	7.93	—	0.00	0	n	
139	13 34 51.27	37 40 51.30	1.23	14.46	17.14	—	0.00	0	n	Outside Chandra FOV
141	13 34 51.86	38 06 35.33	1.78	12.18	4.16	—	22.80	1	n	
144	13 34 53.13	37 48 18.85	1.76	7.59	3.59	—	24.06	2	y	
147	13 34 54.55	37 42 07.32	1.30	13.41	12.44	—	0.00	4	n	
149	13 34 55.11	37 49 51.41	2.44	6.53	2.87	—	25.26	1	n	
150	13 34 55.41	37 50 40.54	2.66	5.96	1.32	—	24.95	4	n	
151	13 34 56.39	37 39 54.75	2.06	15.63	15.15	—	24.89	0	n	Outside Chandra FOV
153	13 34 56.71	37 50 25.09	1.74	6.32	4.97	—	0.00	0	n	
154	13 34 56.76	37 56 03.31	1.48	4.59	3.04	—	20.66	0	n	
155	13 34 56.87	37 52 48.73	2.34	4.94	0.63	—	25.00	0	n	
159	13 34 58.11	37 57 33.15	1.22	5.40	3.34	—	0.00	0	n	
160	13 34 58.14	37 50 52.22	2.32	6.22	1.16	—	0.00	1	n	
163	13 34 59.48	37 57 39.65	1.17	5.69	7.07	—	26.38	2	n	
172	13 35 05.13	37 45 27.22	1.90	11.26	3.52	—	0.00	0	n	
177	13 35 07.69	37 48 27.88	2.66	9.24	2.74	—	25.23	0	n	
179	13 35 09.25	38 04 01.91	1.55	11.43	6.08	—	0.00	1	n	
182	13 35 12.27	37 48 54.89	1.86	9.62	1.73	—	24.32	0	n	
185	13 35 14.41	37 49 12.11	1.49	9.78	20.46	9.2±0.4	20.55	0	n	
194	13 35 17.03	37 49 13.98	14.06	10.19	1.44	—	19.44	15	n	Large error circle
205	13 35 24.72	37 51 24.06	1.68	10.57	3.14	—	0.00	0	n	
206	13 35 24.88	37 44 38.51	1.90	14.34	3.94	—	23.41	0	n	
209	13 35 32.22	38 03 39.97	0.70	14.39	238.21	62±104	25.10	0	n	
210	13 35 32.74	37 45 14.16	4.66	15.08	71.49	26±2	22.43	2	n	
211	13 35 33.05	37 48 02.14	1.98	13.50	3.24	—	18.54	1	n	
215	13 35 37.26	37 47 22.80	1.34	14.55	5.96	—	20.28	0	n	
217	13 35 39.37	37 56 14.96	0.68	12.92	20.15	—	20.89	0	n	Outside Chandra FOV
218	13 35 42.49	37 55 42.93	0.59	13.49	23.77	—	19.47	0	n	Outside Chandra FOV
219	13 35 43.17	37 52 58.65	1.72	13.74	6.49	—	26.58	1	n	Chandra 102 is ~ 10'' North
220	13 35 43.26	37 53 24.27	2.17	13.70	3.95	—	25.89	0	n	Chandra 102 is ~ 15'' South
225	13 35 58.70	37 54 06.31	2.76	16.68	17.44	6.8±1.2	17.51	0	n	Outside Chandra FOV

**Table 5.** Properties of XMM-Newton sources not found in the *Chandra* catalogue of McHardy et al. (2003). The XMM-Newton flux is in units of  $10^{-15}$  erg cm $^{-2}$  s $^{-1}$ . The extension of the source (if applicable) in the XMM-Newton image in units of arcsec. The column marked ‘Chandra counts’ gives the number of counts detected within the XMM-Newton error circle in the *Chandra* image. Excess emission associated with a possible faint source is indicated by a ‘y’ in column 10. See the main text for further details.

<i>Chandra</i> No.	XMM-Newton offaxis angle (arcsec)	0.5–7 keV Flux	Faint XMM-Newton source?	Comments
82	7.0	1.16	y	9'' away from <i>Chandra</i> 28/XMM-Newton 50.
91	12.5	0.94	y	Below final threshold.
96	13.0	0.91	y	18'' away from <i>Chandra</i> 77/XMM-Newton 99.
102	13.0	0.80	y	Between XMM-Newton 219 and XMM-Newton 220. (11'' and 15'' away respectively).
115	11.8	0.70	y	7'' away from <i>Chandra</i> 107/XMM-Newton 214
121	10.4	0.66	n	
145	10.3	0.53	y	9'' away from <i>Chandra</i> 61/XMM-Newton 171.
149	7.1	0.50	y	15'' away from <i>Chandra</i> 23/XMM-Newton 39.
154	11.7	0.47	n	
158	11.5	0.46	y	13'' away from <i>Chandra</i> 117/XMM-Newton 78.
159	6.5	0.45	y	11'' away from <i>Chandra</i> 20/XMM-Newton 175.
163	12.1	0.43	y	
164	10.9	0.43	n	
171	8.6	0.37	n	
181	3.9	0.33	n	
182	11.6	0.32	y	Below final threshold.
183	7.4	0.31	y	Below final threshold.
185	7.0	0.31	y	
188	7.0	0.29	y	14'' away from <i>Chandra</i> 52/XMM-Newton 43.
192	4.3	0.27	y	Below final threshold.
193	2.4	0.27	y	Below final threshold.
195	8.0	0.27	n	
197	7.5	0.26	y	Below final threshold.
198	5.5	0.26	n	
201	3.9	0.24	n	
203	3.8	0.23	y	12'' away from <i>Chandra</i> 108/XMM-Newton 103. In a region of extended emission.
204	7.4	0.23	y	18'' away from <i>Chandra</i> 10/XMM-Newton 119.
205	3.3	0.23	n	
206	7.7	0.23	y	7'' away from <i>Chandra</i> 142/XMM-Newton 128.
207	7.8	0.22	n	
208	7.4	0.21	n	
210	1.0	0.19	y	Below final threshold.
211	9.5	0.19	y	
213	7.2	0.19	y	40'' away from <i>Chandra</i> 28/XMM-Newton 50,

**Table 6.** List of *Chandra* sources with no XMM-Newton counterpart. The *Chandra* flux is in units of  $10^{-15}$  erg cm $^{-2}$  s $^{-1}$ . Excess emission associated with a possible faint source is indicated by a ‘y’ in column 4. The comment ‘Below final threshold’ indicates a source which was detected with EMLDETECT with DET<sub>ML</sub>>5 but subsequently excluded from the final sourcelist according to the criteria in Section 3.2.

clear optical counterpart or counterparts within the positional error radius of the source. Those sources which have optical counterparts extended beyond 10'' are shown in wider images covering 30'' $\times$ 30'' below the main image. Those in the top panel have the same greyscale applied as in the main image, however in the lower panel the greyscale has been individually adjusted for greater clarity. Searching out to a radius of 3'' the number of sources with possible optical counterparts is increased to 58. Of the 9 sources on the edge of, or outside, the *Chandra* field of view, 7 have an optical counterpart.

Table 5 lists the basic properties of the 70 XMM-Newton sources without *Chandra* counterparts. The *Chandra* mosaic image was visually inspected at the positions of each XMM-Newton source to see if any faint X-ray emission could be seen that was not formally detected in the *Chandra* source searching. Details of the number of counts observed within the XMM-Newton positional error circle for each source are listed in column 10 and further comments are listed in column 11. Of the 61 sources not formally detected within the *Chandra* field of view, faint emission is visible in

11 cases. None of the extended XMM-Newton sources are detected with *Chandra*. The XMM-Newton observations are more sensitive to faint extended sources than the *Chandra* observations. One example is the *ROSAT* source R117 (McHardy et al. 1998) which was detected with XMM-Newton (number 56) but missed by *Chandra*. This source is a faint starburst galaxy with extended emission, probably on the scale of the galaxy (Gunn et al. 2001).

Conversely, there are 34 *Chandra* sources with no XMM-Newton counterparts (within the XMM-Newton FOV). The properties of these sources are summarised in Table 6. Seven of these sources were originally detected in our initial XMM-Newton sourcelist, but removed from our final sourcelist after we applied the DET<sub>ML</sub> cutoffs derived in Section 3.2. Visual inspection of the XMM-Newton images at the remaining 27 *Chandra* source positions, suggests a faint source in 16 cases. As well as the 4 close (<10'') pairs of sources found with *Chandra* there are also 9 faint sources which were missed with XMM-Newton because they are in the wings of much brighter sources. This highlights the impor-

tance of our *Chandra* coverage in order to obtain accurate source positions.

## 5 DISCUSSION

### 5.1 Source density in the 13<sup>H</sup> field

Our 13<sup>H</sup> field represents one of the deepest blank field surveys with XMM-*Newton* and as such it is ideal for the investigation of faint X-ray source counts. Further, this work is the only XMM-*Newton* based survey published to date to incorporate detailed Monte-Carlo modelling of the detection process allowing accurate fitting of the source counts. Our source counts are inconsistent with *both* a single and double powerlaw fit in all energy bands, except for our lowest energy band (0.2–0.5 keV) where a double powerlaw fit is acceptable. However, a double powerlaw fit provides a better representation of the source counts according to the KS test in all but our hardest (5–10 keV) energy band where we are unable to constrain the break.

Previous studies show a consensus in shape: the measured source counts are described by a double powerlaw distribution flattening below a flux of  $\sim 1 \times 10^{-14}$  erg cm $^{-2}$  s $^{-1}$  and steeper than an Euclidean slope at fluxes above the break ( $S > S_{\text{knee}}$ ). However the measured normalisations differ by up to  $\sim 30\%$  (Brandt et al. 2001; Rosati et al. 2002). Yang et al. (2003) attribute this field-to-field variation to the fact that the fields studied cover small areas and are subject to cosmic variance. Here the underlying clustered large scale structure imprints a variation in source density on small scales.

The slope of our soft band (0.5–2 keV) source counts, below the break flux of  $1.08^{+1.02}_{-0.39} \times 10^{-14}$  erg cm $^{-2}$  s $^{-1}$ , is consistent with recent determinations using *Chandra* (Rosati et al. 2002; Bauer et al. 2004; Yang et al. 2004). Our 13<sup>H</sup> field is the richest X-ray blank field observation reported to date in this energy band. Our overall normalisation is higher, though consistent with, the CDF-N results of Brandt et al. (2001) and the HELLAS2XMM counts of Baldi et al. (2002). However, the CDF-S source counts of Rosati et al. (2002), and the observed counts in the Lockman hole (Hasinger et al. 1998, 2001) are lower by  $\sim 30\%$ . Allowing for the errors on the CDF-S source counts, given by Rosati et al. (2002), and Poisson errors on our counts, our field is still inconsistent with the CDF-S at the  $2.7\sigma$  level. It is likely therefore that cosmic variance has an important effect on the measured source counts found in deep X-ray fields.

In the 2–5 keV energy band our observed counts are consistent with previous *Chandra* and XMM-*Newton* studies (Brandt et al. 2001; Hasinger et al. 2001; Rosati et al. 2002; Baldi et al. 2002; Cowie et al. 2002; Yang et al. 2004). Our brightest source is a factor of  $\sim 10\times$  fainter than the limiting fluxes of the serendipitous ASCA surveys (Cagnoni, Della Ceca & Maccacaro 1998; Ueda et al. 1999,a) which makes comparisons difficult. However, the ASCA fits of Cagnoni, Della Ceca & Maccacaro (1998) appear to be consistent with ours when extrapolated to the flux range covered by our survey. Our overall normalisation at faint fluxes is closer to the CDF-S normalisation than it is to that found in the CDF-N in this energy band. However, the CDF-S counts drop far more rapidly than ours towards brighter fluxes.

In our hardest energy band (5–10 keV) the observed counts are consistent with a Euclidean slope;  $\gamma = 2.80^{+0.67}_{-0.55}$ . The slope agrees within the errors with the results of Cagnoni, Della Ceca & Maccacaro (1998), Fiore et al. (2001),

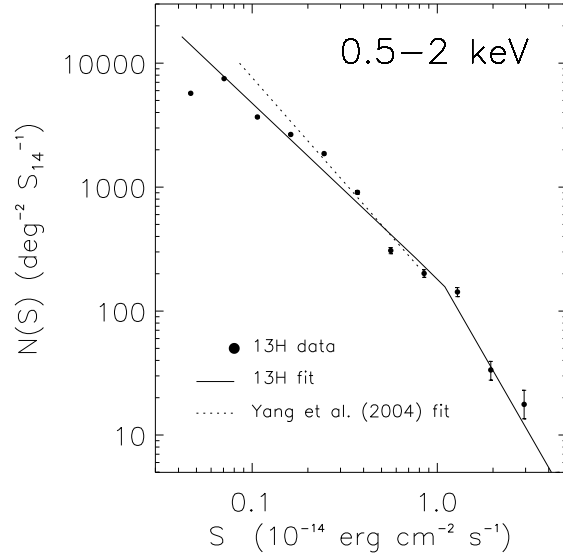


**Figure 12.** 0.5–2 keV energy band differential  $N(S)$  distribution. Overlaid is our double powerlaw fit (solid line). Significant excesses over the model distribution occur at a flux of  $\sim 2 \times 10^{-15}$  erg cm $^{-2}$  s $^{-1}$ . Also shown is the best fit model from the *Chandra* Survey of the Lockman Hole-Northwest (Yang et al. 2004), which covers a similar flux range as our survey (dotted line).

Baldi et al. (2002) and the XMM-*Newton* 5–10 keV counts in the Lockman hole (Hasinger et al. 2001). We expect a break in the source counts at a flux of  $\sim 4 \times 10^{-15}$  erg cm $^{-2}$  s $^{-1}$  as reported from *Chandra* observations of the CDF-S (Rosati et al. 2002). It is therefore unsurprising that it is not detected in our survey, as we have no sources below this flux in our 5–10 keV sourcelist. At the brightest fluxes our counts are in agreement with findings from the HELLAS2XMM survey (Baldi et al. 2002), *BeppoSAX* counts (Fiore et al. 2001) and *ASCA* counts (Cagnoni, Della Ceca & Maccacaro 1998).

Although improved upon a single powerlaw, the double powerlaw fit to the source counts is formally rejected in all but the softest energy band (0.2–0.5 keV). The differential counts show more clearly where the deviations from the model occur and are illustrated in Fig. 12 and Fig. 13. There is an excess over the fit at a flux of  $\sim 2 \times 10^{-15}$  erg cm $^{-2}$  s $^{-1}$  in both the 0.5–2 keV and 2–5 keV energy bands. The fact that this excess is seen in both energy bands suggests that the feature is most likely due to clustering in the field rather than the X-ray spectral properties of the sources around this flux. We defer a study of clustering to a later paper (Loaring et al. 2005).

We have also compared our source counts with wider area *Chandra* surveys which we expect to provide a more accurate value of the global source counts. In the 0.5–2 keV energy band our fits to the differential counts are similar to the fits obtained for the Lockman Hole-Northwest field (Yang et al. 2004). This implies therefore that the CDF-S is a particularly underdense region. In the 2–5 keV energy band our double powerlaw fit lies above the fit of Cowie et al. (2002) which was obtained from the source counts in the CDF-S, CDF-N, and two Hawaii survey fields (SSA13 and SSA22) observed with *Chandra*. If the CDF-S data is excluded from their analysis their faint end normalisation agrees very well with ours, again suggesting that the CDF-S is underdense. This

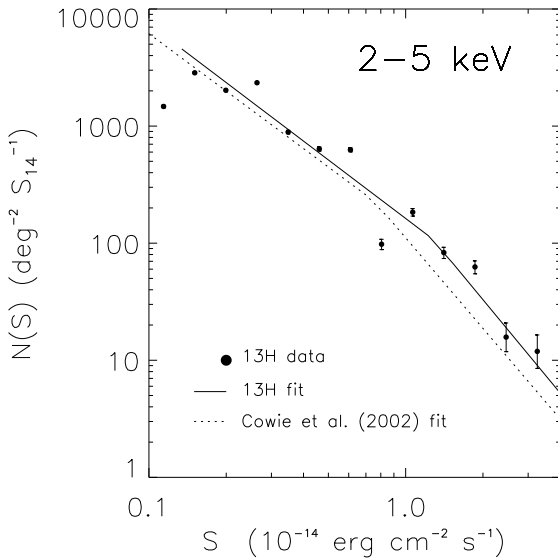


**Figure 13.** 2-5 keV energy band differential  $N(S)$  distribution. Our best fit double powerlaw fit is overlaid (solid line). Significant excesses over the model distribution occur at a flux of  $\sim 3 \times 10^{-15}$  and  $\sim 2 \times 10^{-14}$   $\text{erg cm}^{-2} \text{s}^{-1}$ . The best fit model of Cowie et al. (2002) is also overlaid (dotted line) which is based upon fits to the combined *Chandra* deep field counts and Hawaii survey fields SSA22 and SSA13.

appears to contradict the earlier comparisons between the integral 2-5 keV band counts in which our faint end normalisation closely matches the fits from Rosati et al. (2002). However, the Rosati et al. (2002) CDF-S counts clearly drop below ours at fluxes  $> 5 \times 10^{-15}$   $\text{erg cm}^{-2} \text{s}^{-1}$  and it is at fluxes above the knee that our counts are most discrepant from Cowie et al. (2002). The comparisons depend upon the adopted conversion between instrument energy bands and also the range over which fitting is performed. Rosati et al. (2002) fit to much fainter fluxes than Cowie et al. (2002). As the source counts flatten at faint fluxes this would result in an apparently higher normalisation at brighter fluxes and may explain why the Rosati et al. (2002) normalisation is higher than the Cowie et al. (2002) normalisation at fluxes around  $2 \times 10^{-15}$   $\text{erg cm}^{-2} \text{s}^{-1}$ .

In converting values from the literature into our energy bands we have used a photon index of  $\Gamma = 1.7$  which represents the average slope of the XRB in the 0.2-12 keV energy range. Other authors have chosen to either use individual photon indices measured from their sources (Brandt et al. 2001) or a relatively flat  $\Gamma = 1.4$  (Rosati et al. 2002) which represents the overall XRB spectral slope. Cowie et al. (2002) use a photon index of  $\Gamma = 1.2$  as they assume that the absorbed population must be significantly harder than the unabsorbed population to produce the overall XRB spectrum. However, this photon index appears to be inappropriate at the fluxes probed by our survey. Considering the results from our X-ray spectroscopy (Page et al. 2003, 2005), the vast majority of sources have X-ray spectra with a softer photon index than  $\Gamma = 1.2$ , although they may be absorbed in the soft band. In fact the value of the photon index used has little effect on source counts. Using a photon index of 1.2 and 1.7 respectively to convert the 2-8 keV counts of Cowie et al. (2002) into our 2-5 keV energy band results in a *integral* normalisation difference of  $\sim 13\%$  at our faintest fluxes ( $2.2 \times 10^{-15}$   $\text{erg cm}^{-2} \text{s}^{-1}$ ): counts derived assuming  $\Gamma = 1.7$  are higher than those assuming  $\Gamma = 1.2$ . This direct conversion does

R magnitude	Expected number	Observed number
18–19	0.5	10
19–20	1.1	11
20–21	2.4	18
21–22	5.3	14
22–23	11.7	61
23–24	26.1	54
24–25	57.7	42
25–26	127.7	34

**Table 7.** The number of XMM-Newton optical counterparts as a function of R magnitude. X-ray – optical cross matching was carried out within the 95% positional error circle of each XMM-Newton source and the number of optical detections are displayed as a function of R magnitude. Also shown is the number of expected chance coincidences within each R magnitude interval given the optical source counts of McHardy et al. (2003).

not account for the fact that the original measured fluxes would have been derived from count rates using different photon indices. We have investigated this effect further using spectra which were simulated in XSPEC using the *Chandra* ACIS-I response matrix. Assuming photon indices of  $\Gamma = 1.7$  and  $\Gamma = 1.2$  respectively to convert count rates to fluxes, we obtain a flux ratio  $F_{1.7}/F_{1.2}$  of 0.9 in the 2-5 keV energy band. Incorporating this factor into our flux conversions reduces the apparent normalisation difference to  $\sim 3\%$  at a flux of  $2.2 \times 10^{-15}$   $\text{erg cm}^{-2} \text{s}^{-1}$  (with the normalisation of the  $\Gamma = 1.7$  source counts higher than that of the  $\Gamma = 1.2$  source counts). This factor is not large enough to account for the measured differences in normalisation in the 2-5 keV energy band. It is not necessary to employ any flux conversions for the 0.5-2 keV energy band. However, there is still a  $\sim 30\%$  discrepancy in source counts between the deep fields surveyed to date. One concern is the cross-calibration between the different instruments used. However, ASCA and *Chandra* fluxes agree at about 10% and *Chandra* and XMM-Newton fluxes agree at the 5% level, and so the differences in normalisation cannot be attributed to instrument calibration offsets (Snowden 2001). In the 0.5-2 keV band, we are confident that the field-to-field variations observed are real and due to cosmic variance.

We find a larger field-to-field variation in the soft band (0.5-2 keV) source counts than in the hard band counts (2-5 keV). These findings are at odds with the recent clustering measurements of Yang et al. (2003) who find hard band sources to be more strongly clustered than soft band sources. Further, Gilli et al. (2005) have found no significant difference in clustering strength between soft and hard sources. At present the evidence for any variation in clustering strength due to X-ray hardness appears inconclusive. Clearly larger datasets are required to investigate this issue further. Comparisons with wide area XMM-Newton and *Chandra* serendipitous surveys coupled with further blank field observations should provide sufficient signal to make significant advances in this area.

## 5.2 Survey reliability and capabilities

Our survey was specifically designed to study the X-ray source population within one decade in flux either side of the break in the source counts. Contrary to recent deep *Chandra* surveys we aim not to resolve the entire XRB but rather to determine the dominant emission mechanisms and amount of absorption in these faint sources. To this end we require high quality X-ray spectra, in par-

Radio Flux (mJy)	Expected number	Observed number
50–100	$3.1 \times 10^{-3}$	1
10–50	$4.4 \times 10^{-2}$	0
5–10	$1.8 \times 10^{-2}$	0
1–5	0.3	3
0.5–1	0.1	4
0.1–0.5	3.3	18
0.05–0.10	2.0	6

**Table 8.** The number of XMM-Newton radio counterparts as a function of radio flux. Radio – optical cross matching was carried out within the 95% positional error circle of each XMM-Newton source and the number of radio detections are displayed as a function of radio flux. Also shown is the number of expected chance coincidences given the best-fit radio source count model of Seymour et al. (2004).

ticular at hard energies to probe the absorbed population. The high throughput of XMM-Newton at hard energies makes it particularly suited to this kind of study.

To efficiently study the faint source population we require a highly reliable source catalogue with minimal spurious source contamination. We have examined the quality of our final catalogue via extensive Monte-Carlo simulations (Section 3). Employing the likelihood cutoffs in each energy band determined in Section 3.2 we expect only 7 spurious sources to remain in our final source catalogue. Measurements of the fraction of flux amplified sources in our simulations indicate that confusion is unimportant ( $< 2\%$  of our sources are confused in all energy bands) at the fluxes probed by this survey. This is confirmed via our a cross-correlation with the *Chandra* catalogue of McHardy et al. (2003). We find that only 2% of our sources have ambiguous *Chandra* counterparts.

The average input and output fluxes from our simulations at bright fluxes agree to within 1%. This has important consequences for the determination of source counts, and suggests any systematic deviation between input and output source counts should be very small. Our simulations demonstrate that Eddington bias affects our measured source counts by at most 23 per cent at the faintest fluxes. However, we correct for the effects of Eddington bias when fitting our source counts, using the distribution of  $S_{out}/S_{inp}$  obtained from our simulations, as described in Section 3.3.

Our simulations indicate that the offset in position between input and output sources is less than  $2''$  in 68% of cases within the central  $9'$  of the XMM-Newton field of view (Section 3.1). We therefore expect the majority of our sources to have positions accurate to  $2''$ . However, the EMLDETECT positional errors output from the detection chain are too small and an additional systematic positional error of  $0.76''$  is required (as determined in Section 4.3) to match the real and simulated positional error distributions. The high fidelity of our source positions and fluxes, coupled with insignificant confusion illustrate the high reliability of the survey. We are able to construct useful X-ray spectra down to a 2–5 keV band flux of  $3 \times 10^{-15} \text{ erg cm}^{-2} \text{ s}^{-1}$ , well beyond the initial survey goals (Page et al. 2005).

However, in order to extract the maximum scientific information from the survey, the X-ray sources need to be optically identified, and compared with sources detected in other wavebands, such as our radio source catalogue (Seymour et al. 2004). This requires highly accurate source positions to identify the correct counterpart. The additional systematic positional error has important consequences for optical identification. Using the optical source counts

determined directly within the  $13^H$  field (McHardy et al. 2003) we have calculated the expected number of chance coincidences within an appropriate radius of each source within the field (corresponding to the 95% positional error radius of each source). Table 7 shows the expected number of chance coincidences for the 225 XMM-Newton sources as a function of optical magnitude; it also shows the actual number of optical sources observed within the error circles. X-ray/optical associations at magnitudes  $R \leq 23$  are firm, but approximately half of those at magnitudes  $23 < R < 24$  are likely to be spurious. At fainter magnitudes the majority of optical counterparts are probably unrelated to the X-ray source. This highlights the importance of the *Chandra* coverage over the field which provides accurate X-ray positions and extends the range in which we can correctly select an optical counterpart to a magnitude of  $R = 26$ . This is an issue that must be considered in any deep XMM-Newton survey since if ignored it may lead to a bias in optical identifications. *Chandra* source counts determined by source type find an increasing contribution of absorbed AGN and normal galaxies at the fainter fluxes (Bauer et al. 2004). This suggests that broad line AGN, which dominate at brighter fluxes, are most likely to be correctly identified even without *Chandra* positions. However, in an XMM-Newton survey of similar or greater depth than ours, *Chandra* coverage is essential to identify correctly the optical counterparts of the faintest sources, which are more likely to be associated with absorbed AGN or normal galaxies.

We have carried out a similar comparison with the  $13^H$  field radio catalogue of Seymour et al. (2004). The predicted number of chance coincidences (as predicted from the best-fit starburst and AGN population model of Seymour et al. 2004) are compared with the observed number of radio counterparts in Table 8. We are able to securely identify the correct radio counterpart to a radio flux of 0.1 mJy without *Chandra* positions. Below this flux, we need *Chandra* positions in order to reliably identify real associations between X-ray and radio sources. The relative ease of the identification of radio counterparts compared with that of optical counterparts is due to the paucity of the radio source population.

Eddington bias most affects our counts at faint fluxes, where the statistical errors on our fluxes are largest. For XMM-Newton surveys with shorter exposure times, source counts at faint fluxes will be significantly affected by Eddington bias. Eddington bias at a particular flux depends on the relative errors on the flux, and upon the slope and normalisation of the source counts distribution (Eddington 1913; Teerikorpi 2004). At a flux of  $10^{-15} \text{ erg cm}^{-2} \text{ s}^{-1}$  the relative difference in signal to noise between exposures of 120 and 40 ks is  $\sim 1.7$ . Given that our source counts are boosted by  $\sim 10\%$  at  $3 \times 10^{-15} \text{ erg cm}^{-2} \text{ s}^{-1}$  we expect the source counts in a survey with a 40 ks exposure time to be boosted by  $\sim 29\%$  at  $3 \times 10^{-15} \text{ erg cm}^{-2} \text{ s}^{-1}$ . This is of particular relevance to shallower surveys such as the HELLAS2XMM survey (Baldi et al. 2002), which should be heavily affected by Eddington bias at faint fluxes.

### 5.3 Contribution to the XRB

In this section we examine what fraction of the XRB we can probe with our survey by comparing the integrated emission from our source counts with various measurements of the XRB intensity. To obtain the total 1–2 keV emission from point sources, we integrate our 0.5–2 keV differential source counts between fluxes of  $2 \times 10^{-16} \text{ erg cm}^{-2} \text{ s}^{-1}$  and  $3 \times 10^{-14} \text{ erg cm}^{-2} \text{ s}^{-1}$ ; for fluxes greater than  $3 \times 10^{-14} \text{ erg cm}^{-2} \text{ s}^{-1}$  we have added the integrated counts obtained from the RIXOS survey (Mason et al. 2000). In the 1–2 keV

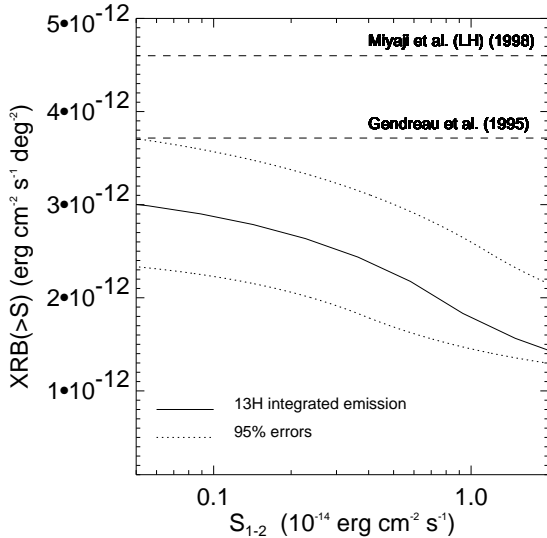


**Figure 14.** Discrete source contribution to the 1-2 keV X-ray background from  $0.1 - 1.0 \times 10^{-13}$  erg cm $^{-2}$  s $^{-1}$ . The solid curve shows the integrated emission from the best fit to our source counts, the dotted curves indicate the lower and upper 95% error on the integrated emission. Measurements of the XRB intensity taken from the literature are overlaid and labelled for comparison. Our source counts account for 47 – 92% of the XRB intensity in this energy band.

band our source counts account for 51–100% of the XRB intensity. Our contribution to the XRB as a function of flux is illustrated in Fig. 14. The main uncertainty in the resolved fraction lies in the range of reported values for the absolute normalisation of the XRB which are discrepant by up to 30%. The XRB measurements of Gendreau et al. (1995) and Vecchi et al. (1999) are taken to represent the lower and upper normalisations respectively in this energy band.

In Fig. 15 we show the contribution of our sources to the integrated 2-5 keV XRB intensity. We integrated our differential source counts between fluxes of  $2 \times 10^{-15}$  erg cm $^{-2}$  s $^{-1}$  and  $1 \times 10^{-13}$  erg cm $^{-2}$  s $^{-1}$  but this time we added on the integrated counts of Cagnoni, Della Ceca & Maccacaro (1998). With respect to the XRB measurements of Gendreau et al. (1995) and Vecchi et al. (1999), our source counts contribute 50–93% of the XRB intensity in the 2-5 keV band. Our source counts would account for the whole 2-5 keV XRB intensity measured by Marshall et al. (1980). Therefore, the XRB intensity within the  $13^H$  field must be higher than that measured by Marshall et al. (1980). Indeed, given that our source counts are rich around  $S_{knee}$ , the XRB intensity within the  $13^H$  field may be somewhat higher than the global average.

We have high quality X-ray spectra to 2-5 keV fluxes of  $3 \times 10^{-15}$  erg cm $^{-2}$  s $^{-1}$  (Page et al. 2003, 2005). At these fluxes we have already resolved  $\sim 30\%$  of the XRB, and hence the  $13^H$  survey is readily suitable for the study of the nature and physical properties of the major XRB producing populations.

## 6 CONCLUSIONS

In this paper we have presented the complete catalogue of 225 sources in the XMM-Newton  $13^H$  deep field which covers a sky

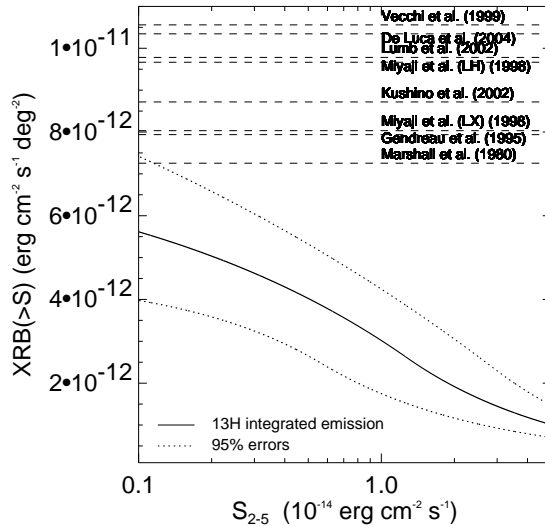


**Figure 15.** Discrete source contribution to the 2-5 keV X-ray background from  $0.1 - 1.0 \times 10^{-13}$  erg cm $^{-2}$  s $^{-1}$ . The solid curve shows the integrated emission from the best fit to our source counts, the dotted curves indicate the lower and upper 95% error on the integrated emission. Measurements of the XRB intensity taken from the literature are overlaid and labelled for comparison. Our source counts account for 42 – 92% of the XRB intensity in this energy band.

area of  $0.18 \text{ deg}^2$  centred on position  $13^{\text{h}} 34^{\text{m}} +37^\circ 53'$ . We reach source densities of  $700 \text{ deg}^{-2}$  at a flux of  $4.1 \times 10^{-16}$  erg cm $^{-2}$  s $^{-1}$  in our lowest energy band. In the 0.5-2 keV band we find source densities of 1300 at a limiting flux of  $4.5 \times 10^{-16}$  erg cm $^{-2}$  s $^{-1}$ . At harder energies we reach fluxes a factor  $\sim 10\times$  brighter, with source densities of 900 and  $300 \text{ deg}^{-2}$  at limiting fluxes of  $1.1 \times 10^{-15}$  erg cm $^{-2}$  s $^{-1}$  and  $5.3 \times 10^{-15}$  erg cm $^{-2}$  s $^{-1}$  in the 2-5 keV and 5-10 keV energy bands respectively.

We have carried out extensive simulations of the detection process in order to assess the reliability of our source catalogue. Simulations indicate that confusion is small ( $< 2\%$ ) in our images. We have curtailed the sourcelist directly derived from the SAS according to the optimal statistical detection likelihoods in each band determined from our simulations. We expect  $< 7$  spurious sources to remain in the final catalogue.

Within the central  $9'$  of the XMM-Newton field of view, positional errors are less than  $2''$  for 68% of our simulated sources and our input/output fluxes agree to within 1% at bright fluxes. Comparison of the input/output source positional offsets from our simulations with the positional offsets found between the XMM-Newton and *Chandra* counterparts suggest that an additional systematic error of  $0.76''$  should be added in quadrature to the EMLDETECT positional errors. This poses no problem for radio counterpart identification. We match our catalogue with the radio catalogue of Seymour et al. (2004) and are confident in our choice of radio counterpart to a flux of 0.1 mJy. In the optical we are confident in our choice of optical counterparts to a magnitude of  $R = 23$  using our XMM-Newton positions. For magnitudes fainter than this we need *Chandra* positions which allow reliable identification of optical counterparts to  $R = 26$  (McHardy et al. 2003).

We have computed the best-fit parameters for the differential  $N(S)$  function using a method adapted from Murdoch et al. (1973).

In all but our hardest energy band the data are described by a double powerlaw model with a break flux at  $\sim 10^{-14}$  erg cm $^{-2}$  s $^{-1}$ . The counts below the break are flatter than the Euclidean case. Our measured source counts are in broad agreement with previous determinations from the *Chandra* deep fields (Brandt et al. 2001; Rosati et al. 2002), XMM-Newton (Hasinger et al. 2001; Baldi et al. 2002) and *BeppoSAX* (Fiore et al. 2001) surveys. The overall normalisation in the 0.5-2 keV band is similar to, though higher than, that found in the CDF-N survey (Brandt et al. 2001). Both the CDF-S (Rosati et al. 2002) and Lockman hole (Hasinger et al. 2001) normalisations are significantly lower than found here. This field-to-field variation in source density may be attributed to the underlying clustered large scale structure which imprints a variation in source density on small scales.

In the 2-5 keV band our faint end normalisation is consistent with the CDF-N (Brandt et al. 2001), CDF-S (Rosati et al. 2002) and XMM-Newton Lockman hole counts (Hasinger et al. 2001). There is minimal flux overlap with the *ASCA* surveys (Cagnoni, Della Ceca & Maccacaro 1998; Ueda et al. 1999,a). The 2-5 keV band *ASCA* counts lie above those found in this survey (Cagnoni, Della Ceca & Maccacaro 1998) although they are still consistent with our model fits. In our hardest energy band (5-10 keV) our counts are in broad agreement with those from *BeppoSAX* and *ASCA*, and with the 5-10 keV counts in the Lockman hole (Hasinger et al. 2001). Again there is little overlap with the brighter *ASCA* and *BeppoSAX* surveys.

The sources in our survey straddle the break in the source counts. Accounting for the uncertainty in our source counts and the absolute normalisation of the XRB we resolve 51-100(50-93)% of the 1-2 (2-5) keV XRB emission. At the break in the source counts we resolve  $\sim 30\%$  of the 2-5 keV XRB. At these fluxes we have X-ray spectra and are therefore able to study the emission mechanisms and investigate absorption in a significant fraction of the X-ray source population.

## REFERENCES

- Alexander D.M. et al., 2001, AJ 122, 2156  
 Alexander D.M. et al., 2003, AJ 126, 539  
 Akiyama M. et al., 2000, ApJ 532, 700  
 Antonucci R.R.J. & Miller J.S., 1985, ApJ, 297, 621  
 Baldi A. et al., 2002, ApJ 564, 190  
 Barger A.J., Cowie L., Mushotzky R. & Richards E., 2001, AJ, 121, 662  
 Barger A.J. et al., 2002, AJ 124, 1839  
 Barger A.J. et al., 2003, AJ 126, 632  
 Bauer F. E. et al, 2004, AJ 128, 2048  
 Brandt W.N. et al., 2001, AJ, 122, 2810  
 Cagnoni I., Della Ceca R. & Maccacaro T., 1998, ApJ 493, 54  
 Carrera F. J., Page M. J. & Mittaz J. P. D., 2004, A&A 420, 163  
 Cash W., 1979, ApJ 228, 939  
 Comastri A., Setti G., Zamorani G. & Hasinger G., 1995, A&A, 296, 1  
 Comastri A. et al., 2001, MNRAS 327, 781  
 Condon J. J., 1974, ApJ 188, 279  
 Cowie L. L. et al., 2002, ApJ, 566, L5  
 Della Ceca et al., 2004, A&A 428, 383  
 De Luca A. & Molendi S., 2004, A&A 419, 837  
 Eddington A. S., 1913, MNRAS 73, 359  
 Fiore F. et al., 1999, MNRAS 306, L55  
 Fiore F. et al., 2001, MNRAS 327, 771  
 Gendreau et al., 1995, PASJ 47, L5  
 Georgantopoulos I. et al., 1997, MNRAS 291, 203  
 Giacconi R. & Zamorani G., 1987, ApJ 313, 20  
 Giacconi R. et al., 2001, ApJ 551, 624  
 Giedke K. et al., 2003, AN 324, No. 1-2, 136  
 Gilli R., Risaliti G. & Salvati M.m 1999, A&A 347, 424  
 Gilli R., Salvati M. & Hasinger G., 2001, A&A 366, 407  
 Gilli R., et al., 2005, A&A 430, 811  
 Giommi P., Perri M. & Fiore F., 2000, A&A 362, 799  
 Gunn K. F. et al., 2001, MNRAS 324, 305  
 Hasinger G. et al., 1993, A&A 275, 1  
 Hasinger G. et al., 1998, A&A 329, 482  
 Hasinger G. et al., 2001, A&A 365, L45  
 Ishisaki Y. et al., 2001, PASJ 53, 445  
 Kirch M., 2004, XMM-SOC-CAL-TN-0018  
 Lamer G. et al., 2003, AN 324, No. 1-2, 16  
 Lehmann I. et al., 2001, A&A 371, 833  
 Loaring N. S., Page M. J. & Ramsay G., 2003, MNRAS 345, 865  
 Loaring N. S. et al., 2005, in prep.  
 Lumb D.H., Warwick R.S., Page M., De Luca A., 2002, A&A 389, 93  
 Maccacaro T. et al., 1991, ApJ 374, 117  
 Madau P., Ghisellini G., & Fabian A.C., 1994, MNRAS 270, L17  
 Mainieri V. et al., 2002, A&A 393, 425  
 Maiolino R. et al., 2001a, A&A, 365, 28  
 Manners J. C. et al., 2003, MNRAS 343, 293  
 Marshall F.E. et al., 1980, ApJ 235, 4  
 Mason K. O., et al., 2000, MNRAS 311, 456  
 Mateos S. et al., (2005), A&A 433, 855  
 McHardy I.M. et al., 1998, MNRAS 295, 641  
 McHardy I.M. et al., 2003, MNRAS 342, 802  
 Murdoch H.S., Crawford D.F & Jauncey D.L., 1997, ApJ 183, 1  
 Mushotzky R.F., Cowie L.L., Barger A.J. & Arnaud K.A., 2000, Nature 404, 459  
 Osborne J., 2001, SSC-LUX-TN-0059 (issue 2), <http://xmmsc-www.star.le.ac.uk/pubdocs/SSC-LUX-TN-0059.ps.gz>  
 Page M.J., Mittaz J. P. D. & Carrera F. J., 2001, MNRAS 325, 757  
 Page M.J. et al. 2003, AN 324, 101  
 Page M. J. et al., 2005, in prep.  
 Rosati P. et al., 2002, ApJ 566, 667  
 Schmidt M. et al., 1998, A&A 329, 495  
 Schwartz D.A., Murray S.S & Gursky H., 1976, ApJ 204, 315  
 Setti G. & Woltjer L., 1989, A&A 224, L21  
 Seymour N., McHardy I. M. & Gunn, K. F., 2004, MNRAS 352, 131  
 Shanks T. et al., 1991, Nature 353, 315  
 Snowden S., 2001, <http://xmm.gsfc.nasa.gov/docs/xmm/estec2001/ccf>  
 Szokoly G. P. et al, 2003, astro-ph/0312324  
 Teerikorpi P., 2004, A&A 424, 73  
 Tozzi P. et al., 2001, ApJ, 562, 42  
 Turner M.J.L. et al., 2001, A&A, 265, L27  
 Ueda Y. et al., 1998, Nature 391, 866  
 Ueda Y. et al., 1999, ApJ 518,656  
 Ueda Y. et al., 1999, ApJ 524, L11  
 Ueda Y. et al., 2001, ApJS 133, 1  
 Vecchi et al., 1999, A&A, 349, L73  
 Voges et al., 1999, A&A 349, 389  
 Yang Y. et al., 2003, ApJ 585, L85  
 Yang Y. et al., 2004, AJ 128, 1501  
 Zamorani G. et al., 1999, A&A 346, 731

Table 9:  $13^H$  XMM-Newton deep field catalogue. All fluxes are in units of  $10^{-15}$  erg cm $^{-2}$  s $^{-1}$ . The columns labelled ‘Counts’ and ‘Counts error’ give the best fit number of source counts and the  $1\sigma$  error as output from EMLDETECT. Flux errors are at  $1\sigma$  confidence. If in any energy band there are fewer counts at the source position in the image than in the background map, then the number of source counts and the source flux are recorded as zero for that band. In this case the ‘Counts error’ and ‘Flux error’ columns represent the  $1\sigma$  upper limit. The ‘Pos error’ column gives the EMLDETECT positional error ( $1\sigma$ ) in arc seconds. The ‘Offaxis angle’ column gives the XMM-Newton offaxis angle in arc minutes. The ‘Chandra No.’ column gives the Chandra catalogue number taken from McHardy et al. (2003). The ‘Chandra offset’ column gives the offset in position between the XMM-Newton and Chandra source, in arcsec.

No.	XMM-Newton			0.2-0.5 keV		0.5-2.0 keV		2.0-5.0 keV		5.0-10.0 keV		0.2-0.5 keV		0.5-2.0 keV		2.0-5.0 keV		5.0-10.0 keV		0.2-10.0 keV					
	Ra J(2000)	Dec J(2000)	Pos <sup>a</sup> error	Offaxis <sup>b</sup> angle	Counts	Counts	Counts	Counts	Counts	Counts	Flux	Flux	Flux	Flux	Flux	Flux	Flux	Flux	Chandra No. <sup>c</sup>	Chandra offset <sup>d</sup>					
						error	error	error	error	error	error	error	error	error	error	error	error	error	error	error					
1	13 33 28.96	37 55 58.82	1.57	12.91	20.08	5.87	55.01	9.56	13.04	6.11	1.36	3.16	3.39	0.99	6.80	1.18	2.89	1.35	1.78	4.12	14.86	4.60			
2	13 33 30.32	37 56 12.21	2.38	12.67	14.12	5.70	22.65	6.82	8.47	5.14	0.00	5.05	1.93	0.78	2.37	0.71	1.65	1.00	0.00	5.44	5.94	5.63			
3	13 33 30.68	37 55 05.57	3.04	12.53	2.06	3.29	23.89	7.07	0.00	3.95	0.00	2.40	0.25	0.40	2.30	0.68	0.00	0.72	0.00	2.42	2.55	2.64			
4	13 33 32.24	37 58 15.92	1.33	12.67	0.00	2.20	42.24	8.16	52.13	9.52	3.62	5.30	0.00	0.16	2.60	0.50	6.77	1.24	2.32	3.39	11.68	3.65	47	1.29	
5	13 33 34.66	37 49 10.68	1.27	13.08	22.60	5.06	49.76	8.22	19.01	6.10	1.49	3.24	2.61	0.58	5.54	0.92	5.36	1.72	1.67	3.63	15.18	4.17	49	2.70	
6	13 33 35.69	37 54 05.50	1.55	11.57	106.05	15.85	306.23	21.37	254.86	20.87	72.68	20.88	3.05	0.46	8.10	0.57	15.76	1.29	19.06	5.48	45.97	5.67	62	5.23	
7	13 33 37.23	37 56 32.06	0.84	11.35	81.88	10.87	110.92	13.68	21.43	7.56	0.00	3.25	2.30	0.30	2.86	0.35	1.28	0.45	0.00	0.83	6.44	1.05	105	2.14	
8	13 33 37.76	37 47 57.33	1.08	13.14	21.87	5.95	48.89	7.40	19.53	6.64	0.00	6.43	2.23	0.60	4.85	0.73	5.02	1.71	0.00	6.50	12.10	6.79	73	2.99	
9	13 33 38.80	37 52 13.60	1.20	11.26	8.75	6.56	66.97	11.82	51.59	10.47	23.63	10.23	0.24	0.18	1.71	0.30	3.06	0.62	5.92	2.56	10.93	2.66	51	4.18	
10	13 33 38.91	38 01 56.15	4.82	12.96	11.17	5.97	22.25	7.95	0.09	2.86	7.08	6.63	0.93	0.50	1.61	0.58	0.01	0.45	5.31	4.98	7.88	5.06			
11	13 33 40.70	37 49 47.79	1.99	11.74	7.54	6.10	38.28	9.47	5.97	7.26	0.00	5.99	0.22	0.18	1.05	0.26	0.38	0.46	0.00	1.63	1.65	1.72			
12	13 33 40.93	37 52 41.26	0.85	10.75	57.69	10.14	102.27	12.83	41.02	10.27	1.50	4.91	1.53	0.27	2.49	0.31	2.32	0.58	0.35	1.16	6.69	1.36	143	2.26	
13	13 33 42.47	38 03 35.94	0.61	13.39	186.82	22.76	287.06	28.25	76.01	15.52	9.65	9.54	18.28	2.23	24.83	2.44	14.59	2.98	8.78	8.68	66.48	9.75	2	1.37	
14	13 33 42.61	37 50 27.06	0.76	11.12	29.36	7.59	107.61	13.18	23.33	7.59	15.49	8.60	0.83	0.21	2.79	0.34	1.41	0.46	3.94	2.19	8.96	2.27	79	1.56	
15	13 33 42.83	37 52 39.90	1.18	10.39	0.66	3.44	76.20	11.52	19.45	7.71	10.21	8.28	0.02	0.09	1.80	0.27	1.06	0.42	2.32	1.88	5.20	1.95	113	1.27	
16	13 33 42.98	37 56 36.73	0.44	10.24	48.93	9.69	446.69	23.94	150.48	15.39	12.43	8.40	1.25	0.25	10.51	0.56	8.21	0.84	2.81	1.90	22.79	2.17	27	1.61	
17	13 33 43.36	37 45 14.61	1.26	13.95	17.98	5.28	45.76	8.11	22.47	7.39	6.39	7.09	1.52	0.45	3.34	0.59	3.53	1.16	4.82	5.36	13.21	5.53	46	2.77	
18	13 33 43.79	37 54 55.76	2.56	9.94	12.00	6.49	34.76	9.48	0.71	4.00	2.67	5.62	0.30	0.16	0.81	0.22	0.04	0.21	0.59	1.25	1.74	1.29			
19	13 33 44.43	37 57 53.49	0.38	10.26	353.57	21.39	422.51	23.96	103.76	13.33	11.93	8.58	9.03	0.55	9.90	0.56	5.62	0.72	2.69	1.94	27.24	2.21	29	1.95	
20	13 33 45.45	37 58 08.04	0.92	10.14	128.52	15.44	114.80	15.21	14.87	8.98	9.44	8.43	3.25	0.39	2.66	0.35	0.80	0.48	2.11	1.88	8.82	2.01			
21	13 33 46.61	38 00 21.56	0.74	10.85	21.83	7.18	170.94	15.57	62.32	11.11	11.40	7.61	0.69	0.23	4.89	0.45	4.06	0.72	3.16	2.11	12.80	2.28	78	0.76	
22	13 33 47.52	37 53 51.50	1.11	9.27	33.80	8.58	45.73	10.90	0.00	7.31	8.14	8.38	0.80	0.20	1.00	0.24	0.00	0.37	1.66	1.71	3.46	1.78			
23	13 33 48.28	37 53 33.71	0.64	9.16	13.48	6.96	50.72	10.11	199.75	16.71	48.63	10.97	0.32	0.17	1.11	0.22	10.05	0.84	9.97	2.25	21.45	2.42	76	0.66	
24	13 33 48.60	37 58 07.79	0.57	9.55	146.08	14.13	166.80	15.63	43.17	9.69	5.77	6.80	3.56	0.34	3.75	0.35	2.25	0.50	1.22	1.44	10.78	1.61	40	1.25	
25	13 33 50.68	37 49 46.61	0.85	10.01	19.02	7.54	132.61	14.58	45.80	10.49	3.45	5.66	0.48	0.19	3.05	0.34	2.44	0.56	0.75	1.24	6.72	1.41	128	1.36	
26	13 33 50.80	37 57 16.61	1.77	8.88	8.66	6.42	25.68	8.03	32.51	9.23	11.06	7.91	0.20	0.15	0.53	0.17	1.56	0.44	2.15	1.53	4.43	1.61			
27	13 33 53.59	38 02 03.64	0.77	10.73	42.68	8.30	117.78	13.64	18.24	7.38	11.30	8.55	1.15	0.22	2.91	0.34	1.04	0.42	2.71	2.05	7.81	2.13	72	1.29	
28	13 33 54.21	38 02 53.17	1.23	11.21	35.02	8.06	16.36	7.20	12.39	6.80	32.15	9.36	1.64	0.38	0.67	0.30	1.11	0.61	13.07	3.81	16.49	3.89			
29	13 33 54.91	37 51 25.87	1.81	8.50	17.87	6.74	33.18	9.28	0.00	5.35	0.00	5.89	0.39	0.15	0.67	0.19	0.00	0.25	0.00	1.09	1.06	1.14	175	3.41	
30	13 33 55.88	37 52 57.85	0.28	7.81	227.18	16.97	636.62	26.92	196.33	16.74	75.24	12.65	4.87	0.36	12.55	0.53	8.87	0.76	13.42	2.26	39.71	2.46	17	1.04	
31	13 33 57.90	37 49 59.01	2.91	8.70	20.13	7.65	25.94	9.21	0.00	2.37	0.00	2.55	0.45	0.17	0.53	0.19	0.00	0.11	0.00	0.48	0.98	0.56			
32	13 33 58.56	37 59 37.55	0.23	8.46	478.40	23.67	1031.89	34.31	320.33	20.81	70.33	12.92	10.84	0.54	21.58	0.72	15.50	1.01	13.59	2.50	61.51	2.84	7	0.75	
33	13 33 58.87	38 00 24.88	1.17	8.87	13.57	6.81	30.94	8.16	22.51	7.78	14.47	8.31	0.44	0.22	0.90	0.24	1.43	0.50	3.83	2.20	6.60	2.28			
34	13 33 59.21	38 05 58.32	1.37	13.03	7.77	4.94	17.99	5.00	18.54	6.00	1.12	3.23	1.06	0.67	1.88	0.52	3.62	1.17	1.21	3.49	7.78	3.78	111	3.20	

Continued on next page

No.	XMM-Newton		0.2-0.5 keV		0.5-2.0 keV		2.0-5.0 keV		5.0-10.0 keV		0.2-0.5 keV		0.5-2.0 keV		2.0-5.0 keV		5.0-10.0 keV		0.2-10.0 keV					
	Ra J(2000)	Dec J(2000)	Pos <sup>a</sup> error	Offaxis <sup>b</sup> angle	Counts	Counts error	Counts	Counts error	Counts	Counts error	Flux	Flux error	Flux	Flux error	Flux	Flux error	Flux	Flux error	Flux	Chandra No. <sup>c</sup>	offset <sup>d</sup>			
	35	13 33 59.56	37 51 39.75	2.34	7.57	5.28	6.21	36.92	10.18	9.90	7.53	5.15	6.68	0.11	0.12	0.68	0.19	0.42	0.32	0.86	1.11	2.06	1.18	
36	13 33 59.63	37 49 26.35	12.19	8.75	0.00	4.59	90.42	19.99	0.00	5.21	0.00	7.12	0.00	0.10	1.86	0.41	0.00	0.25	0.00	1.35	1.86	1.44		
37	13 34 00.04	37 49 12.27	0.32	8.84	373.03	20.83	712.58	28.63	131.11	14.00	3.02	5.26	8.45	0.47	14.86	0.60	6.31	0.67	0.58	1.01	30.21	1.44	4	1.49
38	13 34 00.91	38 01 25.24	0.95	9.24	5.46	5.57	88.41	12.16	44.95	10.00	8.60	7.99	0.13	0.13	1.92	0.26	2.25	0.50	1.75	1.63	6.06	1.73	84	0.51
39	13 34 01.05	37 54 03.99	0.35	6.60	244.79	17.97	549.22	25.28	261.35	19.83	76.08	13.84	4.95	0.36	10.35	0.48	11.50	0.87	12.64	2.30	39.45	2.53	23	1.00
40	13 34 01.06	38 00 25.75	1.50	8.55	6.96	6.07	19.52	7.67	58.74	10.85	11.63	7.96	0.17	0.15	0.43	0.17	2.94	0.54	2.38	1.63	5.92	1.73		
41	13 34 01.26	37 46 47.56	0.90	10.41	8.67	6.83	147.83	15.54	59.26	11.84	14.80	8.84	0.23	0.18	3.55	0.37	3.31	0.66	3.40	2.03	10.48	2.18	48	1.05
42	13 34 02.62	37 51 29.14	0.36	7.12	144.04	14.09	419.12	22.19	99.91	13.25	21.77	9.24	2.80	0.27	7.52	0.40	4.12	0.55	3.47	1.48	17.92	1.65	43	0.88
43	13 34 03.09	37 53 21.42	0.50	6.34	2.26	4.13	95.74	12.95	287.86	19.70	90.74	13.78	0.04	0.08	1.62	0.22	11.20	0.77	13.50	2.05	26.36	2.20	52	0.58
44	13 34 07.18	37 59 59.34	1.23	7.36	18.32	10.34	0.00	3.70	45.94	14.61	15.40	10.88	0.37	0.21	0.00	0.07	1.93	0.62	2.57	1.81	4.87	1.93		
45	13 34 08.05	38 06 26.62	0.92	12.62	33.53	7.81	94.69	12.52	6.79	7.46	33.96	10.12	1.29	0.30	3.29	0.43	0.54	0.59	12.00	3.58	17.12	3.67	60	1.39
46	13 34 08.36	37 52 19.21	0.50	5.72	115.74	12.85	256.77	18.53	73.97	11.86	28.75	9.60	2.01	0.22	4.12	0.30	2.71	0.43	4.00	1.34	12.84	1.45	68	1.08
47	13 34 08.39	37 47 50.85	2.69	8.72	5.54	6.28	15.49	8.33	34.65	10.02	13.50	8.48	0.12	0.14	0.32	0.17	1.66	0.48	2.56	1.61	4.67	1.69		
48	13 34 08.59	37 54 40.76	0.53	5.06	94.30	12.27	234.91	18.41	118.64	15.53	13.93	8.44	1.56	0.20	3.58	0.28	4.10	0.54	1.83	1.11	11.08	1.28	58	1.38
49	13 34 08.72	38 03 49.23	0.47	10.22	112.09	12.97	331.70	21.03	43.75	10.19	12.05	9.31	2.94	0.34	7.99	0.51	2.44	0.57	2.80	2.16	16.16	2.32	25	1.01
50	13 34 08.79	37 57 06.43	0.27	5.47	249.06	17.77	860.91	31.47	287.71	20.38	88.02	13.60	4.29	0.31	13.63	0.50	10.37	0.73	12.13	1.87	40.42	2.10	28	0.45
51	13 34 09.96	37 54 31.62	0.78	4.80	0.82	3.39	23.43	9.06	128.60	14.47	47.77	11.24	0.01	0.06	0.35	0.14	4.38	0.49	6.15	1.45	10.89	1.53	141	0.82
52	13 34 10.61	37 59 56.03	0.31	6.84	641.48	29.15	351.57	22.04	94.69	12.23	15.53	9.25	17.53	0.80	8.66	0.54	5.18	0.67	3.43	2.04	34.80	2.35	9	0.46
53	13 34 11.42	37 47 57.32	0.51	8.29	172.60	15.68	234.29	18.23	62.26	10.90	20.36	9.54	3.72	0.34	4.66	0.36	2.85	0.50	3.68	1.73	14.92	1.87	66	1.76
54	13 34 12.36	37 59 10.36	2.01	6.06	28.74	11.66	0.00	3.54	0.00	5.63	3.76	5.90	0.53	0.22	0.00	0.06	0.00	0.22	0.56	0.88	1.10	0.94		
55	13 34 13.03	37 58 31.63	0.77	5.52	81.50	11.53	147.43	14.16	43.77	9.56	10.94	8.25	1.85	0.26	3.02	0.29	1.97	0.43	1.94	1.47	8.79	1.58	85	0.71
56	13 34 13.59	37 45 39.06	1.22	10.12	32.55	8.52	65.93	10.90	0.00	2.05	0.00	5.19	0.84	0.22	1.57	0.26	0.00	0.11	0.00	1.18	2.42	1.23		
57	13 34 13.62	38 07 23.60	0.89	13.12	23.57	7.54	195.39	17.42	69.29	11.80	13.87	9.29	0.83	0.26	6.28	0.56	5.18	0.88	4.59	3.08	16.89	3.26	88	1.66
58	13 34 14.15	38 04 41.20	1.00	10.54	9.96	6.36	75.06	12.90	95.57	13.20	29.41	9.64	0.27	0.17	1.86	0.32	5.46	0.75	7.09	2.32	14.67	2.47	132	1.35
59	13 34 14.37	37 52 32.09	1.43	4.59	0.00	1.14	37.94	8.56	19.46	8.35	0.00	6.75	0.00	0.03	0.84	0.19	0.93	0.40	0.00	1.27	1.77	1.34	119	1.03
60	13 34 14.79	37 59 59.67	0.85	6.36	50.74	10.19	130.43	14.39	22.30	8.86	17.50	8.82	0.97	0.19	2.29	0.25	0.89	0.35	2.71	1.37	6.86	1.45	120	1.20
61	13 34 14.81	37 51 30.81	0.38	5.12	206.64	15.92	353.49	21.06	0.00	2.77	0.00	3.77	3.48	0.27	5.49	0.33	0.00	0.10	0.00	0.50	8.98	0.67	81	0.12
62	13 34 15.49	38 03 05.78	1.80	8.97	11.63	6.18	13.12	7.94	32.35	9.58	13.20	8.16	0.27	0.14	0.28	0.17	1.60	0.47	2.66	1.64	4.81	1.72		
63	13 34 15.54	37 52 27.80	1.31	4.43	0.00	1.52	43.88	14.26	65.88	11.49	19.04	9.60	0.00	0.03	0.68	0.22	2.32	0.40	2.53	1.28	5.54	1.36		
64	13 34 17.01	37 59 48.75	0.96	5.95	48.10	9.74	87.75	12.41	22.14	8.52	1.93	5.23	0.87	0.18	1.46	0.21	0.84	0.32	0.28	0.77	3.45	0.87	170	0.72
65	13 34 17.51	37 57 21.91	0.14	4.10	1590.56	41.23	2266.48	49.01	681.39	28.69	136.27	15.72	25.25	0.65	33.02	0.71	22.45	0.95	16.96	1.96	97.67	2.38	5	0.64
66	13 34 17.80	37 44 31.39	2.04	10.89	3.97	5.25	23.78	9.25	43.92	10.78	0.00	7.79	0.12	0.15	0.64	0.25	2.76	0.68	0.00	2.03	3.51	2.16		
67	13 34 18.87	37 58 56.69	0.32	5.04	18.29	6.88	403.89	22.27	415.62	22.78	110.89	13.89	0.31	0.12	6.34	0.35	14.87	0.81	15.03	1.88	36.56	2.08	63	0.76
68	13 34 19.24	37 43 49.99	1.55	11.47	0.00	3.55	37.29	9.86	32.42	9.24	17.94	9.22	0.00	0.11	1.02	0.27	2.08	0.59	4.84	2.49	7.94	2.57	137	1.79
69	13 34 19.26	37 50 29.60	0.52	5.32	105.10	13.16	217.42	17.46	67.50	11.43	19.94	9.27	1.87	0.23	3.56	0.29	2.51	0.43	2.81	1.31	10.75	1.42	116	1.40
70	13 34 19.56	37 51 47.77	1.40	4.26	0.00	5.64	22.75	8.79	43.62	10.11	14.49	8.37	0.00	0.09	0.33	0.13	1.45	0.34	1.80	1.04	3.58	1.10		
71	13 34 19.97	37 54 00.29	0.61	2.96	23.51	7.43	170.55	15.77	63.23	10.82	27.08	8.46	0.41	0.13	2.70	0.25	2.23	0.38	3.60	1.12	8.94	1.22	93	0.66
72	13 34 20.80	37 59 30.74	0.96	5.30	11.54	6.63	25.22	8.81	91.13	12.72	24.21	8.82	0.20	0.12	0.41	0.14	3.38	0.47	3.41	1.24	7.40	1.34	191	1.72
73	13 34 20.82	37 54 59.88	0.50	2.64	99.21	12.17	201.23	16.48	80.58	11.46	11.53	7.36	1.59	0.20	2.96	0.24	2.66	0.38	1.43	0.91	8.64	1.03	59	1.30
74	13 34 21.90	38 04 50.89	1.34	10.22	13.39	6.83	70.31	10.93	17.24	8.12	0.00	4.95	0.36	0.18	1.71	0.27	0.97	0.46	0.00	1.17	3.03	1.29	133	0.61
75	13 34 22.07	37 53 46.31	1.73	2.66	4.71	5.74	38.37	9.96	16.37	8.21	7.01	7.76	0.07	0.08	0.52	0.13	0.50	0.25	0.79	0.88	1.88	0.93	196	0.99
76	13 34 22.11	37 48 03.61	1.88	7.26	6.37	6.82	10.70	7.81	51.41	10.64	29.54	10.23	0.13	0.14	0.20	0.14	2.17	0.45	4.84	1.68	7.33			

No.	XMM-Newton		Pos <sup>a</sup> error	Offaxis <sup>b</sup> angle	0.2-0.5 keV		0.5-2.0 keV		2.0-5.0 keV		5.0-10.0 keV		0.2-0.5 keV		0.5-2.0 keV		2.0-5.0 keV		5.0-10.0 keV		0.2-10.0 keV			
	Ra J(2000)	Dec J(2000)			Counts	Counts error	Counts	Counts error	Counts	Counts error	Counts	Counts error	Flux	Flux error	Flux	Flux error	Flux	Flux error	Flux	Flux error	Flux	Flux error		
81	13 34 24.64	37 46 14.71	0.41	8.88	178.04	15.30	348.71	20.78	96.94	13.23	37.19	10.82	4.30	0.37	7.75	0.46	4.98	0.68	7.64	2.22	24.67	2.40	38	0.71
82	13 34 25.91	37 54 59.89	1.58	1.64	14.36	7.19	43.44	10.29	19.36	9.08	2.68	5.84	0.20	0.10	0.57	0.13	0.57	0.27	0.29	0.64	1.63	0.71		
83	13 34 26.87	38 00 27.92	1.45	5.73	7.55	6.69	48.90	9.81	0.00	3.17	12.04	7.98	0.13	0.12	0.80	0.16	0.00	0.12	1.73	1.14	2.66	1.17		
84	13 34 27.39	37 50 08.65	0.63	4.96	11.89	6.93	184.42	16.61	81.70	11.58	33.24	9.46	0.20	0.12	2.88	0.26	2.91	0.41	4.44	1.26	10.43	1.36	71	1.59
85	13 34 28.44	37 47 08.21	1.37	7.87	34.54	8.19	42.64	9.80	3.53	5.41	11.43	7.83	0.74	0.17	0.84	0.19	0.16	0.24	2.02	1.39	3.76	1.43	122	1.83
86	13 34 28.64	37 41 27.94	1.72	13.50	27.59	7.21	59.37	10.79	3.99	5.16	0.03	3.12	1.42	0.37	2.98	0.54	0.52	0.67	0.02	1.59	4.93	1.85	104	1.22
87	13 34 28.66	37 57 48.26	1.92	3.09	0.12	3.32	19.04	8.81	36.28	9.61	6.56	7.78	0.00	0.05	0.27	0.12	1.16	0.31	0.79	0.93	2.21	0.99		
88	13 34 28.80	37 53 37.96	1.78	1.67	20.62	8.34	34.32	9.32	1.57	4.65	12.52	9.51	0.29	0.12	0.45	0.12	0.05	0.14	1.36	1.04	2.15	1.06		
89	13 34 29.20	38 02 45.33	1.79	7.90	31.01	7.09	5.60	5.78	1.37	4.29	0.00	3.63	0.71	0.16	0.12	0.12	0.07	0.21	0.00	0.70	0.89	0.76		
90	13 34 29.30	38 06 51.45	1.76	11.98	9.93	6.62	62.33	10.73	22.52	9.25	12.33	8.47	0.32	0.21	1.81	0.31	1.52	0.63	3.63	2.50	7.29	2.60		
91	13 34 29.77	37 49 20.20	1.31	5.65	4.60	5.16	49.09	10.08	17.20	7.34	0.00	2.67	0.10	0.11	0.95	0.19	0.75	0.32	0.00	0.45	1.79	0.59	168	1.10
92	13 34 29.93	37 56 38.98	0.56	1.93	9.55	6.82	124.70	14.63	191.02	16.82	71.70	13.02	0.17	0.12	2.05	0.24	6.92	0.61	9.91	1.80	19.05	1.92	80	1.54
93	13 34 30.32	37 55 25.03	0.76	0.92	64.17	10.97	103.10	14.12	47.54	10.59	7.60	8.25	0.89	0.15	1.32	0.18	1.37	0.31	0.81	0.88	4.39	0.96	179	0.26
94	13 34 30.42	37 57 02.31	1.43	2.25	1.45	3.95	57.38	11.71	19.03	8.38	3.74	5.72	0.02	0.06	0.84	0.17	0.62	0.27	0.46	0.70	1.94	0.77	174	1.73
95	13 34 31.27	38 03 10.23	0.82	8.27	11.49	6.28	122.99	14.41	106.97	13.46	14.82	7.77	0.28	0.15	2.84	0.33	5.85	0.74	3.15	1.65	12.12	1.84	69	0.58
96	13 34 31.32	37 49 53.09	0.50	5.07	8.57	5.74	178.97	15.71	116.16	13.15	27.23	8.66	0.16	0.11	3.10	0.27	4.55	0.51	4.06	1.29	11.87	1.42	55	1.10
97	13 34 31.41	37 48 31.24	0.19	6.42	551.25	24.99	1311.70	38.02	557.43	25.96	103.11	13.80	11.42	0.52	25.23	0.73	24.84	1.16	17.41	2.33	78.90	2.75	3	0.78
98	13 34 33.10	37 55 10.22	1.01	0.33	0.72	3.85	14.98	9.14	82.72	13.16	55.10	12.07	0.01	0.05	0.19	0.12	2.38	0.38	5.85	1.28	8.44	1.34	180	1.51
99	13 34 33.51	38 05 41.29	1.60	10.77	1.80	3.50	52.34	9.89	17.55	8.14	0.00	6.97	0.05	0.10	1.37	0.26	1.06	0.49	0.00	1.81	2.49	1.89	162	1.53
100	13 34 33.55	37 48 35.76	1.75	6.32	13.06	9.23	9.47	10.42	64.98	15.75	35.18	12.53	0.27	0.19	0.18	0.20	2.82	0.68	5.87	2.09	9.14	2.22	144	0.49
101	13 34 33.93	38 00 43.04	0.45	5.80	125.34	13.03	236.45	17.79	136.00	14.90	27.63	9.60	2.28	0.24	3.94	0.30	5.14	0.56	4.04	1.40	15.40	1.56	45	1.40
102	13 34 34.02	37 49 46.74	2.30	5.14	0.00	1.14	31.58	8.86	14.42	7.93	0.00	4.35	0.00	0.02	0.52	0.15	0.54	0.30	0.00	0.61	1.06	0.70	209	0.97
103	13 34 34.76	37 56 46.68	1.09	1.86	73.93	14.89	418.91	27.83	137.13	18.61	31.78	13.65	1.08	0.22	5.62	0.37	4.15	0.56	3.57	1.53	14.43	1.69	108	7.54
104	13 34 34.92	38 07 03.03	1.99	12.13	13.92	7.24	53.49	10.86	21.49	8.42	4.41	6.37	0.65	0.34	2.23	0.45	2.00	0.78	1.83	2.64	6.71	2.81		
105	13 34 35.17	37 49 11.83	2.08	5.73	9.81	6.56	39.07	9.92	5.93	6.63	0.00	2.83	0.18	0.12	0.64	0.16	0.22	0.25	0.00	0.40	1.04	0.52	161	0.96
106	13 34 35.27	37 53 55.19	1.23	1.02	20.65	8.42	56.19	11.82	22.31	8.87	0.53	4.23	0.29	0.12	0.72	0.15	0.65	0.26	0.06	0.45	1.71	0.55	212	1.15
107	13 34 35.86	37 54 18.96	0.55	0.68	27.31	9.48	214.46	17.79	145.24	16.18	33.91	10.90	0.38	0.13	2.74	0.23	4.18	0.47	3.60	1.16	10.90	1.28	94	0.34
108	13 34 36.21	37 51 06.68	0.90	3.83	25.90	7.38	89.84	12.65	40.47	9.96	13.00	8.33	0.61	0.17	1.90	0.27	1.86	0.46	2.32	1.49	6.70	1.59	106	0.31
109	13 34 36.36	37 55 57.15	0.27	1.12	0.00	4.40	233.04	24.08	598.14	31.60	192.44	19.25	0.00	0.07	3.31	0.34	18.99	1.00	22.86	2.29	45.16	2.52	26	0.51
110	13 34 36.38	38 05 14.02	1.25	10.32	23.58	7.73	73.39	11.98	39.95	10.10	0.00	4.87	0.70	0.23	1.98	0.32	2.49	0.63	0.00	1.29	5.16	1.49		
111	13 34 36.74	38 03 19.95	0.99	8.43	55.01	9.47	85.94	12.54	18.92	8.57	6.36	7.34	1.27	0.22	1.82	0.27	0.92	0.42	1.26	1.45	5.27	1.55	97	1.21
112	13 34 37.20	37 54 38.28	0.70	0.65	29.01	8.65	35.71	10.52	150.02	16.27	61.36	12.36	0.40	0.12	0.46	0.13	4.33	0.47	6.54	1.32	11.73	1.41	95	1.79
113	13 34 37.91	37 56 04.43	0.15	1.37	1373.41	39.50	2286.52	51.57	954.92	36.56	229.08	20.82	21.18	0.61	32.29	0.73	30.28	1.16	27.05	2.46	110.80	2.88	8	2.09
114	13 34 38.26	38 01 39.25	1.05	6.78	0.00	1.38	66.80	11.81	71.99	11.68	9.09	8.33	0.00	0.03	1.25	0.22	3.06	0.50	1.52	1.40	5.84	1.50	87	1.13
115	13 34 38.41	38 06 26.50	0.48	11.55	122.44	12.95	424.83	24.07	105.52	13.89	43.65	11.47	3.77	0.40	12.00	0.68	6.93	0.91	12.39	3.26	35.09	3.47	33	1.41
116	13 34 38.83	37 40 22.03	1.11	14.58	38.49	13.87	141.83	24.35	61.06	17.94	23.66	15.16	2.34	0.84	8.41	1.44	9.45	2.78	14.58	9.34	34.78	9.88		
117	13 34 38.96	37 42 43.95	1.60	12.22	14.48	7.18	37.60	9.95	20.13	8.29	7.73	8.14	0.48	0.24	1.16	0.31	1.45	0.60	2.40	2.52	5.49	2.62		
118	13 34 39.75	37 57 01.93	1.29	2.38	19.69	8.23	61.75	12.50	19.82	8.07	9.82	8.49	0.30	0.12	0.85	0.17	0.62	0.25	1.14	0.99	2.91	1.04		
119	13 34 41.79	38 00 11.23	0.24	5.48	316.89	19.31	860.60	30.88	318.61	20.12	78.99	12.44	5.97	0.36	14.87	0.53	12.51	0.79	11.94	1.88	45.28	2.14	10	0.55
120	13 34 42.29	37 41 46.46	0.78	13.24	79.19	10.54	209.90	16.62	9.62	7.69	0.2													

No.	XMM-Newton		Pos <sup>a</sup>		Offaxis <sup>b</sup>		0.2-0.5 keV		0.5-2.0 keV		2.0-5.0 keV		5.0-10.0 keV		0.2-0.5 keV		0.5-2.0 keV		2.0-5.0 keV		5.0-10.0 keV		0.2-10.0 keV	
	Ra J(2000)	Dec J(2000)	error	angle	Counts	error	Counts	error	Counts	error	Counts	error	Counts	error	Flux	error	Flux	error	Flux	error	Flux	error	Flux	error
																							Chandra No. <sup>c</sup>	offset <sup>d</sup>
127	13 34 44.15	37 44 35.27	1.80	10.52	2.44	4.28	7.48	7.26	38.12	9.26	6.88	6.78	0.07	0.13	0.20	0.20	2.38	0.58	1.78	1.76	4.44	1.86	130	1.37
128	13 34 45.24	38 00 31.75	0.86	6.02	31.85	8.62	104.55	13.64	54.81	11.17	10.98	8.47	0.62	0.17	1.87	0.24	2.24	0.46	1.74	1.34	6.47	1.45	142	1.97
129	13 34 45.28	37 57 22.73	0.46	3.29	184.76	15.45	294.62	20.08	99.51	13.16	25.56	9.89	2.96	0.25	4.35	0.30	3.33	0.44	3.20	1.24	13.84	1.37	53	0.89
130	13 34 46.31	37 54 42.14	0.48	2.40	45.55	9.43	245.13	17.72	115.17	13.50	24.07	8.11	0.76	0.16	3.74	0.27	3.92	0.46	3.08	1.04	11.51	1.18	65	0.82
131	13 34 46.46	37 58 41.64	1.21	4.48	31.91	9.09	55.76	11.30	21.99	8.45	1.76	4.69	0.58	0.16	0.92	0.19	0.82	0.31	0.25	0.67	2.56	0.78	167	2.46
132	13 34 47.02	37 47 48.76	0.34	7.54	57.55	10.32	607.27	27.42	345.04	21.18	85.21	13.94	1.48	0.26	14.85	0.67	20.44	1.25	18.56	3.04	55.33	3.36	11	0.88
133	13 34 47.18	37 57 14.88	1.53	3.46	10.32	6.95	9.74	8.53	58.46	11.55	11.18	8.99	0.17	0.11	0.15	0.13	1.98	0.39	1.42	1.14	3.71	1.22		
134	13 34 47.34	37 59 50.90	0.29	5.57	104.57	12.72	699.41	29.71	409.45	23.75	83.56	13.61	2.28	0.28	14.03	0.60	18.79	1.09	14.70	2.39	49.79	2.71	13	1.14
135	13 34 48.20	37 51 11.74	1.50	4.63	11.20	6.74	56.93	10.94	39.71	10.05	0.00	2.42	0.19	0.11	0.88	0.17	1.39	0.35	0.00	0.32	2.46	0.52	153	1.65
136	13 34 48.22	37 54 14.33	1.06	2.84	25.88	6.79	29.11	7.96	28.00	7.85	30.38	8.93	0.62	0.16	0.62	0.17	1.28	0.36	5.41	1.59	7.93	1.65		
137	13 34 49.76	37 54 50.58	0.98	3.07	2.48	4.11	79.80	11.34	49.13	10.04	0.00	7.28	0.05	0.08	1.38	0.20	1.88	0.39	0.00	1.06	3.31	1.15	172	1.34
138	13 34 50.53	38 07 05.73	0.90	12.59	74.42	10.91	103.12	12.90	51.01	10.36	9.42	8.59	2.69	0.39	3.41	0.43	3.91	0.79	3.17	2.89	13.18	3.05	92	2.49
139	13 34 51.27	37 40 51.30	1.23	14.46	13.36	6.99	108.01	12.87	71.85	11.81	13.41	8.99	0.57	0.30	4.27	0.51	6.78	1.11	5.52	3.70	17.14	3.91		
140	13 34 51.48	37 46 19.83	0.04	9.24	9433.50	98.55	28488.97	164.27	1707.69	43.33	111.49	14.22	243.71	2.55	676.67	3.90	93.51	2.37	24.68	3.15	1038.57	6.10	1	0.94
141	13 34 51.86	38 06 35.33	1.78	12.18	16.13	7.57	33.62	9.52	36.35	9.84	0.00	3.84	0.54	0.25	1.03	0.29	2.59	0.70	0.00	1.20	4.16	1.44		
142	13 34 52.02	37 58 25.78	0.38	4.96	0.00	2.89	261.59	17.90	329.33	20.63	81.39	12.13	0.00	0.05	4.27	0.29	12.18	0.76	11.53	1.72	27.99	1.90	64	0.34
143	13 34 52.12	37 57 45.06	0.22	4.53	407.05	21.87	816.21	30.82	311.10	20.75	73.48	11.85	6.95	0.37	12.78	0.48	11.03	0.74	9.91	1.60	40.67	1.86	22	0.70
144	13 34 53.13	37 48 18.85	1.75	7.59	0.00	1.02	10.11	7.54	31.08	8.49	9.88	7.21	0.00	0.02	0.21	0.16	1.50	0.41	1.88	1.37	3.59	1.44		
145	13 34 53.79	38 07 54.86	1.23	13.55	59.90	9.57	88.33	12.52	34.72	10.61	12.21	8.88	2.31	0.37	3.12	0.44	2.87	0.88	4.52	3.29	12.82	3.45	109	3.69
146	13 34 53.83	37 51 09.02	1.42	5.40	0.48	3.49	53.31	11.50	46.12	10.42	19.15	9.12	0.01	0.06	0.87	0.19	1.72	0.39	2.71	1.29	5.31	1.36	165	1.32
147	13 34 54.55	37 42 07.32	1.30	13.41	29.77	8.51	59.82	10.07	15.61	8.39	22.16	9.52	1.12	0.32	2.08	0.35	1.28	0.69	7.95	3.41	12.44	3.51		
148	13 34 54.83	37 52 40.44	1.23	4.64	2.55	4.50	27.13	9.02	44.17	10.17	40.10	11.12	0.04	0.08	0.43	0.14	1.57	0.36	5.39	1.50	7.44	1.55	199	2.53
149	13 34 55.11	37 49 51.41	2.44	6.53	8.49	6.07	32.70	9.91	6.55	6.38	10.14	8.04	0.18	0.13	0.64	0.19	0.29	0.29	1.76	1.39	2.87	1.44		
150	13 34 55.41	37 50 40.53	2.66	5.96	9.44	6.60	33.98	10.34	11.04	7.37	0.00	4.53	0.19	0.13	0.64	0.20	0.49	0.33	0.00	0.74	1.32	0.84		
151	13 34 56.39	37 39 54.74	2.06	15.63	51.51	21.81	130.31	32.80	1.88	11.49	0.00	14.54	4.25	1.80	10.50	2.64	0.40	2.43	0.00	12.53	15.15	13.15		
152	13 34 56.63	37 53 50.42	1.14	4.55	30.18	7.85	63.28	11.12	19.67	8.15	0.95	4.21	0.52	0.14	1.01	0.18	0.72	0.30	0.13	0.58	2.38	0.69	150	0.46
153	13 34 56.71	37 50 25.09	1.74	6.32	14.92	7.63	51.12	11.65	5.39	6.11	19.05	8.72	0.33	0.17	1.03	0.23	0.25	0.28	3.37	1.54	4.97	1.59		
154	13 34 56.76	37 56 03.31	1.47	4.59	29.34	7.50	12.78	8.16	16.19	9.10	7.95	8.75	0.66	0.17	0.26	0.17	0.73	0.41	1.39	1.53	3.04	1.60		
155	13 34 56.87	37 52 48.73	2.34	4.94	1.62	4.45	35.09	9.45	0.00	3.90	0.00	1.25	0.03	0.08	0.60	0.16	0.00	0.15	0.00	0.19	0.63	0.30		
156	13 34 56.98	37 45 53.46	2.74	10.09	2.53	4.45	50.36	11.77	7.86	7.45	3.09	5.69	0.07	0.12	1.27	0.30	0.46	0.44	0.74	1.36	2.54	1.47	178	2.24
157	13 34 57.12	37 55 41.16	1.42	4.58	0.00	4.34	44.63	10.13	45.78	9.84	13.29	8.97	0.00	0.08	0.77	0.17	1.80	0.39	1.97	1.33	4.54	1.40	176	1.02
158	13 34 57.56	37 49 43.19	1.22	6.95	9.85	6.12	58.78	11.16	40.17	9.38	24.01	8.84	0.21	0.13	1.15	0.22	1.79	0.42	4.18	1.54	7.34	1.61	112	2.93
159	13 34 58.11	37 57 33.15	1.22	5.40	25.18	6.58	21.53	7.26	3.60	5.02	8.19	7.18	0.74	0.19	0.56	0.19	0.20	0.28	1.84	1.61	3.34	1.66		
160	13 34 58.14	37 50 52.22	2.32	6.22	10.82	6.68	45.71	11.15	0.00	2.71	0.00	3.56	0.24	0.15	0.92	0.22	0.00	0.12	0.00	0.63	1.16	0.69		
161	13 34 58.42	38 04 30.68	0.95	10.71	49.06	9.45	91.85	12.68	23.79	8.49	0.00	4.64	1.44	0.28	2.46	0.34	1.48	0.53	0.00	1.23	5.38	1.41	103	0.95
162	13 34 58.85	37 50 23.08	1.85	6.65	71.22	14.35	258.27	23.32	63.18	15.54	0.00	10.37	1.46	0.30	4.87	0.44	2.71	0.67	0.00	1.73	9.05	1.93	160	5.81
163	13 34 59.48	37 57 39.65	1.17	5.69	28.90	7.93	18.30	7.58	4.26	5.61	24.24	8.64	0.85	0.23	0.48	0.20	0.24	0.32	5.50	1.96	7.07	2.01		
164	13 35 00.07	37 53 45.12	1.18	5.23	36.13	8.33	35.52	9.32	23.31	8.27	8.62	8.07	0.65	0.15	0.59	0.15	0.88	0.31	1.24	1.16	3.36	1.22	177	1.68
165	13 35 00.10	37 56 33.31	0.53	5.36	21.22	6.48	184.76	16.27	159.40	15.48	31.60	10.03	0.39	0.12	3.09	0.27	6.05	0.59	4.60	1.46	14.13	1.60	70	1.25
166	13 35 01.23	37 59 37.81	0.83	7.11	31.51	7.42	79.89	11.09	26.91	8.51	0.00	4.49	0.68	0.16	1.57	0.22	1.21	0.38	0.00	0.80	3.46	0.93	151	0.81
167	13 35 02.01	37 47 24.90	2.63	9.30	0.00	4.96	18.63	8.87	29.65	9.15	1.52	4.48	0.00	0.13	0.43	0.21	1.60</							

XMM-Newton				0.2-0.5 keV		0.5-2.0 keV		2.0-5.0 keV		5.0-10.0 keV		0.2-0.5 keV		0.5-2.0 keV		2.0-5.0 keV		5.0-10.0 keV		0.2-10.0 keV		
No.	Ra J(2000)	Dec J(2000)	Pos <sup>a</sup> error	Offaxis <sup>b</sup> angle	Counts	Counts error	Counts	Counts error	Counts	Counts error	Flux	Flux error	Flux	Flux error	Flux	Flux error	Flux	Flux error	Flux	Chandra No. <sup>c</sup>	offset <sup>d</sup>	
173	13 35 05.61	37 50 31.57	0.99	7.59	64.19	12.11	110.06	16.45	32.94	10.05	16.65	8.21	1.39	0.26	2.20	0.33	1.51	0.46	3.00	1.48	8.11	1.60
174	13 35 05.79	38 07 02.41	1.39	13.62	2.94	4.49	62.97	10.94	27.24	9.73	6.78	8.04	0.12	0.18	2.36	0.41	2.38	0.85	2.65	3.14	7.50	3.29
175	13 35 06.23	37 49 53.20	0.33	8.08	289.05	18.94	509.07	25.29	247.65	18.81	40.68	10.75	6.56	0.43	10.63	0.53	11.88	0.90	7.72	2.04	36.79	2.33
176	13 35 07.16	37 45 43.12	1.90	11.27	23.31	6.74	10.05	7.51	17.18	7.89	0.00	7.44	0.72	0.21	0.28	0.21	1.14	0.52	0.00	2.07	2.14	2.15
177	13 35 07.69	37 48 27.88	2.66	9.24	24.37	8.29	10.46	7.93	6.07	7.07	7.08	7.57	0.62	0.21	0.24	0.19	0.33	0.38	1.54	1.65	2.74	1.72
178	13 35 08.67	37 57 05.14	1.31	7.13	14.35	6.96	58.06	10.67	9.81	7.99	0.00	5.22	0.36	0.17	1.35	0.25	0.53	0.43	0.00	1.09	2.25	1.22
179	13 35 09.24	38 04 01.91	1.55	11.43	20.16	7.23	56.79	10.99	9.95	7.85	10.54	8.52	0.64	0.23	1.66	0.32	0.68	0.53	3.10	2.50	6.08	2.59
180	13 35 09.69	37 50 10.45	2.26	8.46	14.78	7.59	35.54	9.45	5.53	6.41	0.00	4.01	0.35	0.18	0.79	0.21	0.28	0.33	0.00	0.81	1.42	0.92
181	13 35 09.70	37 48 21.20	0.77	9.60	49.75	9.99	106.96	13.36	41.20	9.68	0.00	5.37	1.32	0.26	2.61	0.33	2.33	0.55	0.00	1.23	6.25	1.41
182	13 35 12.27	37 48 54.89	1.85	9.62	13.53	7.61	56.55	12.07	0.00	5.27	0.00	4.22	0.36	0.20	1.37	0.29	0.00	0.30	0.00	0.96	1.73	1.07
183	13 35 12.42	38 02 48.21	0.59	10.90	16.70	6.95	202.22	17.06	102.98	12.87	41.27	10.99	0.52	0.22	5.80	0.49	6.85	0.86	11.76	3.13	24.93	3.29
184	13 35 12.78	37 44 19.98	0.58	13.04	73.12	10.70	146.05	15.02	78.19	12.32	6.21	7.74	2.71	0.40	5.00	0.51	6.32	1.00	2.18	2.71	16.20	2.96
185	13 35 14.41	37 49 12.11	1.49	9.78	180.44	21.04	450.74	32.32	55.29	17.09	5.33	10.96	4.85	0.57	11.17	0.80	3.18	0.98	1.25	2.57	20.46	2.92
186	13 35 14.71	37 52 58.17	1.02	8.22	31.68	9.16	95.09	15.23	48.86	11.11	0.00	4.35	0.76	0.22	2.11	0.34	2.49	0.57	0.00	0.89	5.36	1.13
187	13 35 14.77	37 48 40.89	1.18	10.15	5.56	6.44	74.15	13.31	60.01	10.86	13.17	8.95	0.15	0.18	1.90	0.34	3.57	0.65	3.22	2.19	8.85	2.31
188	13 35 14.85	37 50 37.05	0.99	9.10	4.32	5.09	79.49	12.04	53.72	10.87	6.56	7.45	0.14	0.16	2.29	0.35	3.52	0.71	1.77	2.01	7.72	2.16
189	13 35 14.87	38 03 20.49	2.08	11.62	5.70	5.05	27.83	8.50	13.79	7.65	0.00	2.08	0.20	0.18	0.89	0.27	1.02	0.57	0.00	0.67	2.11	0.94
190	13 35 15.23	37 58 39.44	0.52	8.91	122.14	13.02	214.02	17.32	103.73	13.38	6.05	6.96	3.11	0.33	5.01	0.41	5.60	0.72	1.33	1.53	15.06	1.77
191	13 35 15.79	37 52 17.45	0.65	8.61	22.41	8.75	181.13	18.53	126.77	15.42	28.58	9.46	0.55	0.22	4.12	0.42	6.65	0.81	6.03	2.00	17.35	2.20
192	13 35 15.92	37 52 40.22	0.27	8.53	301.70	19.32	869.40	32.44	358.09	22.56	76.47	12.97	7.44	0.48	19.73	0.74	18.75	1.18	16.10	2.73	62.02	3.10
193	13 35 16.28	37 56 20.95	1.11	8.42	27.09	7.32	65.09	10.80	14.60	7.49	11.92	7.53	0.75	0.20	1.70	0.28	0.92	0.47	2.88	1.82	6.25	1.91
194	13 35 17.03	37 49 13.98	14.06	10.18	0.00	2.79	36.41	12.16	7.99	8.56	0.00	6.90	0.00	0.08	0.95	0.32	0.49	0.52	0.00	1.72	1.44	1.83
195	13 35 17.41	37 54 15.66	0.78	8.54	52.14	9.62	105.80	13.39	63.20	11.13	12.71	8.46	1.32	0.24	2.45	0.31	3.37	0.59	2.74	1.83	9.89	1.96
196	13 35 17.49	38 02 48.32	0.54	11.61	54.00	9.42	248.40	18.10	95.96	12.08	19.82	9.27	1.84	0.32	7.76	0.57	7.00	0.88	6.27	2.93	22.87	3.13
197	13 35 18.36	37 55 40.82	2.29	8.74	11.71	6.64	33.30	8.82	8.82	6.60	6.19	7.26	0.50	0.28	1.26	0.33	0.72	0.54	2.15	2.53	4.63	2.62
198	13 35 18.90	37 54 17.31	1.08	8.84	14.21	7.33	42.89	9.58	53.35	11.27	38.95	9.68	0.36	0.19	1.01	0.23	2.90	0.61	8.59	2.14	12.87	2.24
199	13 35 19.20	37 43 15.73	1.11	14.66	35.19	8.16	85.78	12.37	8.65	7.58	26.92	10.77	1.89	0.44	4.21	0.61	1.00	0.87	13.90	5.56	21.00	5.68
200	13 35 19.43	37 53 00.36	0.92	9.12	12.12	7.32	88.72	11.91	47.35	9.74	22.10	9.13	0.32	0.19	2.13	0.29	2.63	0.54	5.00	2.06	10.08	2.16
201	13 35 19.71	37 49 19.62	1.70	10.58	6.50	5.38	4.79	6.18	44.57	10.68	29.36	10.07	0.19	0.16	0.13	0.17	2.89	0.69	7.84	2.69	11.06	2.79
202	13 35 19.81	37 58 26.53	1.03	9.65	38.19	8.96	86.46	12.35	24.91	8.74	0.00	2.03	1.05	0.25	2.18	0.31	1.46	0.51	0.00	0.49	4.69	0.81
203	13 35 22.90	37 49 12.74	0.73	11.17	0.00	2.48	133.86	13.80	104.04	12.66	14.15	8.54	0.00	0.08	4.11	0.42	7.45	0.91	4.26	2.57	15.83	2.76
204	13 35 24.33	37 46 16.52	0.95	13.14	34.17	8.50	123.43	14.02	30.93	9.89	17.30	9.86	1.29	0.32	4.30	0.49	2.55	0.81	6.19	3.53	14.33	3.67
205	13 35 24.72	37 51 24.05	1.68	10.57	6.72	5.95	41.33	9.07	13.20	8.05	3.51	5.87	0.20	0.18	1.14	0.25	0.85	0.52	0.94	1.58	3.14	1.69
206	13 35 24.88	37 44 38.51	1.90	14.34	18.49	7.33	34.24	9.58	19.28	8.96	0.00	6.46	0.79	0.31	1.35	0.38	1.80	0.84	0.00	2.67	3.94	2.84
207	13 35 25.73	37 52 35.59	1.84	10.43	0.00	3.66	7.89	6.39	38.07	9.72	9.37	7.72	0.00	0.11	0.22	0.17	2.42	0.62	2.49	2.05	5.12	2.15
208	13 35 30.29	37 57 49.58	0.49	11.43	164.89	14.27	333.02	20.63	119.05	13.55	28.51	9.50	5.41	0.47	10.04	0.62	8.39	0.96	8.61	2.87	32.46	3.12
209	13 35 32.22	38 03 39.97	0.70	14.39	341.31	124.60	1118.08	250.31	123.81	85.34	181.69	50.53	23.79	8.68	72.41	16.21	19.24	13.27	122.76	34.14	238.21	40.99
210	13 35 32.74	37 45 14.16	4.66	15.08	147.90	60.71	339.03	68.07	205.01	91.84	0.00	47.49	10.76	4.42	23.82	4.78	36.91	16.54	0.00	35.31	71.49	39.53
211	13 35 33.05	37 48 02.14	1.98	13.50	27.29	7.29	21.51	8.33	6.53	7.07	1.53	4.84	1.16	0.31	0.84	0.33	0.61	0.66	0.63	1.98	3.24	2.14
212	13 35 35.46	37 57 46.54	0.33	12.41	303.12	18.62	628.71	26.87	150.04	15.07	29.36	10.13	11.01	0.68	21.02	0.90	11.78	1.18	10.05	3.47	53.86	3.83
213	13 35 35.71	38 01 50.81	1.01	13.96	0.36	2.91	44.86	9.88	134.88	15.04	43.71	10.81	0.02	0.15	2.23	0.49	17.39	1.94	22.80	5.64	42.44	5.98
214	13 35 35.89	37 51 13.03	1.32	12.72	11.45	6.40	104.41	13.34	82.13	12.56	19.45	9.95	0.43	0.24	3.63	0.46	6.73	1.03	6.93	3.55	17.72	3.73
215	13 35 37.26	37 47 22.79	1.34	14.55	15.37	6.41	49.66	9.67	26.26	9.42	0.69	4.77	0.73	0.30	2.17	0.42	2.73	0.98	0.32	2.21	5.96	2.47
216	13 35 38.71	37 55 12.54	1.82	12.72	4.83	5.58	4.91	6.18	57.52	11.35	15.11	8.36	0.19	0.22	0.17	0.22	4.80	0.95	5.53	3.06	10.69	3.21</

XMM-Newton				0.2-0.5 keV		0.5-2.0 keV		2.0-5.0 keV		5.0-10.0 keV		0.2-0.5 keV		0.5-2.0 keV		2.0-5.0 keV		5.0-10.0 keV		0.2-10.0 keV				
No.	Ra J(2000)	Dec J(2000)	Pos <sup>a</sup> error	Offaxis <sup>b</sup> angle	Counts	Counts error	Counts	Counts error	Counts	Counts error	Flux Flux	Flux error	Flux Flux	Flux error	Flux Flux	Flux error	Flux Flux	Flux error	Chandra No. <sup>c</sup>	offset <sup>d</sup>				
219	13 35 43.17	37 52 58.65	1.72	13.74	27.58	7.83	55.53	11.44	21.22	8.31	0.00	7.15	1.46	0.41	2.67	0.55	2.36	0.93	0.00	3.60	6.49	3.78		
220	13 35 43.26	37 53 24.27	2.17	13.70	21.30	6.79	30.19	9.48	0.00	4.52	2.55	5.04	1.15	0.37	1.48	0.47	0.00	0.51	1.31	2.60	3.95	2.71		
221	13 35 44.64	37 51 41.28	0.41	14.27	270.01	18.90	524.77	25.80	193.88	17.13	33.49	11.30	11.97	0.84	21.47	1.06	18.82	1.66	14.45	4.87	66.71	5.32	12	1.14
222	13 35 45.19	37 49 59.54	1.06	14.85	20.64	7.03	168.87	15.28	83.51	12.07	34.00	10.65	1.23	0.42	9.16	0.83	10.54	1.52	19.68	6.16	40.61	6.42	39	1.86
223	13 35 46.27	37 53 26.79	2.12	14.29	25.41	7.64	25.08	8.82	36.04	10.41	2.94	5.69	1.45	0.44	1.30	0.46	4.34	1.25	1.61	3.13	8.71	3.43	134	3.00
224	13 35 52.53	37 50 51.25	1.57	15.98	6.01	4.84	24.38	8.50	30.85	8.44	12.10	7.68	0.47	0.38	1.88	0.65	6.22	1.70	9.88	6.27	18.45	6.54	114	7.62
225	13 35 58.70	37 54 06.31	2.76	16.68	36.88	9.68	124.62	15.69	9.53	8.54	2.91	5.99	3.02	0.79	9.97	1.26	1.99	1.79	2.45	5.05	17.44	5.56		

## APPENDIX A: SYNTHETIC FIELD GENERATION

### A1 Method

Input sourcelists were generated independently for each of the four energy bands. The differential source count function,  $N(S)$ , was modelled as a broken power law distribution:

$$N(S) = \begin{cases} K_1 \left(\frac{S}{S_{norm}}\right)^{-\gamma_1} & (S < S_{knee}) \\ K_2 \left(\frac{S}{S_{norm}}\right)^{-\gamma_2} & (S \geq S_{knee}) \end{cases} \quad (\text{A1})$$

The normalisation constants were chosen such that the function is continuous at the knee, i.e.  $K_1/K_2 = (S_{knee}/S_{norm})^{\gamma_1-\gamma_2}$ . The parameters selected for the simulations were based on results from the CDF-S (see Rosati et al. 2002). A photon index,  $\Gamma = 1.7$  (approximately that of the XRB in the 0.2–10 keV energy range), was used to convert from the *Chandra* energy bands to the energy bands used in this study. We have slightly modified the *Chandra*  $N(S)$  parameters via an iterative process so that the ‘output’ source counts approximately match those seen in the  $13^H$  field data.

In order to incorporate the effects of source confusion, we set our simulated source flux limits,  $S_{lim}$ , to values approximately five times fainter than the limit reached by the  $13^H$  data. The mean number of input sources per field per energy band,  $\langle N \rangle$ , was calculated by integrating  $N(S)$  from  $S_{lim}$  to infinity. The actual number of sources used in each simulated field was taken randomly from a Poisson distribution about  $\langle N \rangle$ . For each of these sources, a flux was randomly assigned from the appropriate  $N(S)$  distribution. Any input source having a flux greater than twice that of the brightest source in the  $13^H$  data was discarded. This prevented any single simulated field being dominated by an extremely bright source: a situation not seen in the  $13^H$  data. The effects of source clustering are ignored in this analysis, hence each input source was assigned a purely random position within the field. Finally, the source fluxes were converted to count rates.

### A2 Imaging characteristics

To convert the simulated input sourcelists to images, one has to take account of the complex point spread function (PSF) of the EPIC cameras. We used the ‘MEDIUM’ accuracy PSF description (Kirch 2004) from the XMM-Newton calibration files, which is also the model used by the SAS source searching task EMLDETECT. This PSF description consists of a number of small ray-traced maps each describing the PSF at a particular energy and off-axis angle, covering the full EPIC field of view and energy range. These maps were interpolated in energy and off-axis angle, allowing us to evaluate the fraction of any source’s flux within any image pixel. The SAS-generated exposure maps from the  $13^H$  field give the effective exposure times and vignetting corrections for each energy band and EPIC camera. The simulated images were generated pixel by pixel by summing the contribution from all input sources. We added a two-component, (vignetted and un-vignetted), synthetic background to the simulated images to reproduce that observed in the  $13^H$  field. The correct level of this background was determined through an iterative process because undetected, faint simulated sources contribute significantly to the diffuse background. Finally, the value of each pixel was randomly drawn from the appropriate Poisson distribution to simulate photon counting noise.

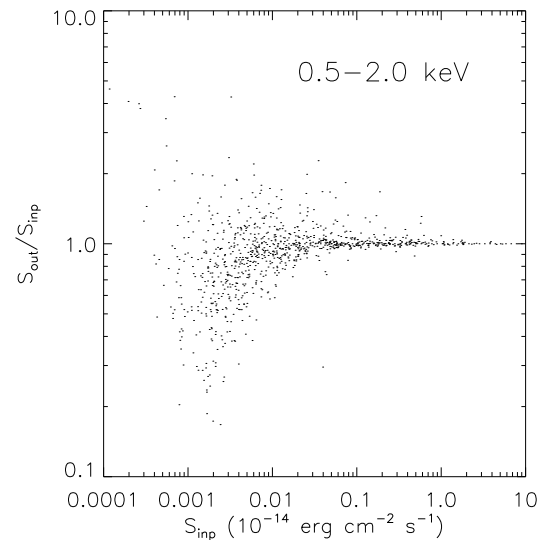


**Figure B1.** Scatter plot of input vs output flux in the 0.5–2 keV energy band. We only show those detected sources having  $\text{DET\_ML} \geq 5$  and valid input counterparts within 5'', 8'', and 10'' for input offaxis angles of 0–9°, 9–12° and > 12° respectively.

### A3 Simulated image analysis

We used a single-band version of the source searching process (as described in Section 2.2) on the simulated images. This process was repeated independently in each of the four energy bands. Two iterations of the background fitting/source finding process were carried out per band per field. The output sourcelist was curtailed at a detection likelihood of  $\text{DET\_ML} = 5$ .

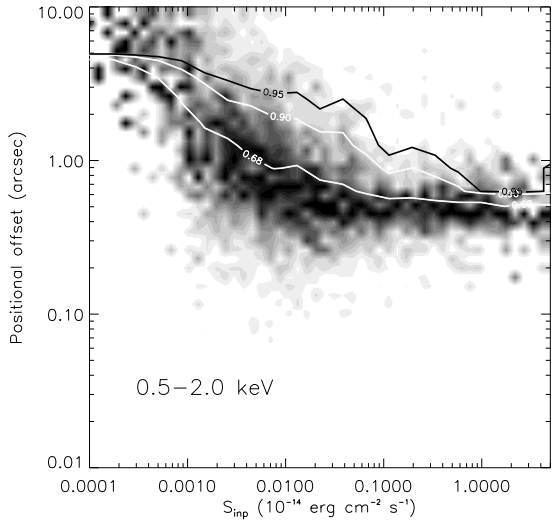
## APPENDIX B: ASSESSING THE IMPACT OF CONFUSION

### B1 Simulation method

In order to investigate the ultimate confusion limit of deep XMM-Newton surveys, we have produced a small number of extremely deep simulations, with exposure times 1000× that of the  $13^H$  field. The input sourcelists reach fluxes of a few  $10^{-19} - 10^{-18}$   $\text{erg cm}^{-2} \text{s}^{-1}$  depending on energy band. No background or Poisson noise were added to the images in these simulations, so differences between the input and output source counts arise solely as a result of confusion. The sources were matched within a cutoff radius,  $r_{cut}$ , which depends on XMM-Newton offaxis angle as described in Section 3.1.

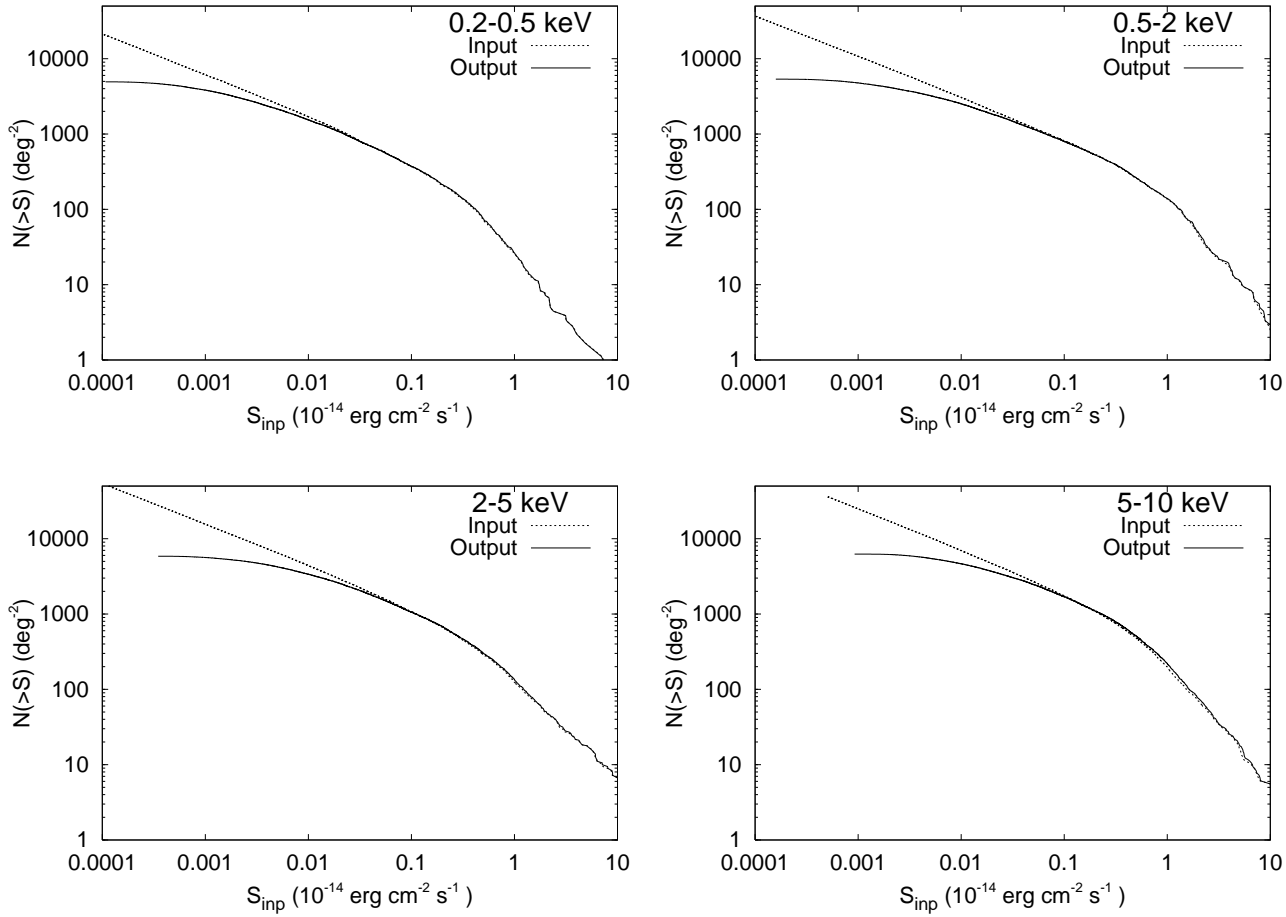
### B2 Results

Fig. B1 shows the distribution of  $S_{out}/S_{inp}$  for our 10 simulations in the 0.5–2 keV energy band. The scatter on  $S_{out}/S_{inp}$  increases dramatically below a flux of  $10^{-16} \text{ erg cm}^{-2} \text{s}^{-1}$ . At similar fluxes, the input-output position offsets, shown in Fig. B2 become much larger. The source density at this flux level is approximately  $2000 \text{ deg}^{-2}$  and represents the limit beyond which source properties cannot be recovered reliably irrespective of exposure time.



**Figure B2.** Greyscale image showing the distribution of positional offsets between output and input source locations as a function of input flux in the 0.5–2 keV energy band. Those sources within the central 9' of the XMM-Newton field of view having  $\text{DET\_ML} \geq 5$  are shown. The concentration of positional offsets as a function of  $S_{\text{inp}}$  is indicated by the darkness of the greyscale image. The three contours show the distances within which 68, 90, and 95 per cent of the data lie.

Fig. B3 show the average input and output integral source counts in each of our four energy bands. The input and output source counts are already discrepant when the source density reaches  $2000 \text{ deg}^{-2}$ , and diverge rapidly at fainter fluxes. The approximate input fluxes corresponding to source densities of  $2000 \text{ deg}^{-2}$  are  $3 \times 10^{-17}$ ,  $10^{-16}$ ,  $2 \times 10^{-16}$  and  $3 \times 10^{-16} \text{ erg cm}^{-2} \text{ s}^{-1}$  in the 0.2–0.5, 0.5–2, 2–5 and 5–10 keV energy bands respectively.



**Figure B3.** Comparison of input (dotted line) and output (solid line) simulated source counts. Input source counts were simulated to fluxes of  $5 \times 10^{-19}$   $\text{erg cm}^{-2} \text{ s}^{-1}$  in the 0.2-0.5 keV and 0.5-2 keV energy bands. In the 2-5 keV and 5-10 keV energy bands the input counts were simulated to fluxes of  $1 \times 10^{-18}$  and  $5 \times 10^{-18}$   $\text{erg cm}^{-2} \text{ s}^{-1}$ . Confusion is evident at faint fluxes where the input and output source counts rapidly diverge.